Energy Management and Control of Electrical Drives in Hybrid Electrical Vehicles

Ottosson, Jonas

2007

CODEN:LUTEDX/(TEIE-1054)/1-132/(2007)

Industrial Electrical Engineering and Automation

Energy Management and Control of Electrical Drives in Hybrid Electrical Vehicles

Jonas Ottosson

Dept. of Industrial Electrical Engineering and Automation
Lund University

Energy Management and Control of Electrical Drives in Hybrid Electrical Vehicles

Jonas Ottosson

LUND UNIVERSITY

Licentiate Thesis
Department of Industrial Electrical Engineering and Automation

2007

Department of Industrial Electrical Engineering and Automation
Lund University
Box 118
SE-221 00 LUND
SWEDEN

http://www.iea.lth.se

ISBN 978-91-88934-46-8
CODEN:LUTEDX/(TEIE-1054)/1-132/(2007)

Printed in Sweden by Media-Tryck, Lund University
Lund 2007

Abstract

Hybrid vehicles have attracted tremendous attention during the last years. Increasing environmental concern and a steady increase in fuel prices are key factors for the growing interest. Hybrid vehicles, which benefits from having at least two different energy converters and two different energy storage systems, have proven to have significant potential to improve fuel economy without reducing the performance of the vehicle. However, the extra degree of freedom inherited by the use of two energy sources on-board the vehicle, gives rise to a more complicated energy management control.

The first part of the thesis treats the subject of energy management in hybrid electrical vehicles. The gain in fuel consumption and the minimization of emissions are highly dependent on the performance of the control strategy. A rather simple heuristic control strategy presented in the literature is optimized. Heuristic control strategies are often referred to as hard to tune, and none optimal. However, the result presented in the thesis shows that the strategy is easily tuned, robust and has no significant cycle-beating trait. Dynamic programming is used to obtain a global optimal solution to the control problem. The result of this global optimization is then used as a basis for evaluating the real-time heuristic control strategy and serves as a lower bound for the fuel consumption for a given cycle. A comparison of fuel consumption for the two control strategies shows that, though being quite simple, the heuristic control strategy gives a relatively near-optimal result.

The second part of the thesis is devoted to the development of an electrically driven rear axle for a HEV in collaboration with SAAB Automobile. A rear drive unit, consisting of an electrical machine, planetary gear and a differential, was provided by SAAB. Focus is on control and thermal modeling of the electrical machine. A simple and effective field weakening controller, giving fast field weakening performance is proposed. The fast field weakening performance is important in a HEV since the battery voltage undergoes rapid variations, during accelerations. In addition to this, the FWC minimizes the torque-per-current ratio by, for a given torque, using the current combination yielding the minimal stator current. In addition to this, a thermal model based on several thermal measurements is proposed and validated against data. The thermal model forms the basis for the derivation of an over temperature controller, preventing the machine from over heating.

Acknowledgements

First, I would like to thank my supervisor Mats Alaküla. I do not know anyone having the ability to encourage people like Mats. I have learnt a lot from him, not just in the technical area. Without his support and enthusiasm, this thesis would never have been possible. I would also like to thank my assistant supervisor Rolf Egnell for his support in the area of combustion engines.

I have spent many hours at SAAB Automobile in Trollhättan and I would like to thank all of the people who I have met during my visits for taking such good care of me, special thanks to Tommy Lindholm, Lars Hoffman, Roland Andersson, Rolf Ottersten, Leif Hermansson and Adam Smith. The cooperation with SAAB Automobile has been very valuable to me.

I would like to thank all the people at the department of Industrial Electrical Engineering and Automation at Lund University for all the amusing discussions and the relaxed atmosphere. Special thanks to Getachew Darge and Bengt Simonsson for helping me out in the lab. I would also like to thank David Dufke for all the help with the CAN-communication. Joakim Larsson and Per Bandrup, your help has been very valuable to me. Last, but definitely not least, I would like to thank my fellow PhD-students Jonas Johansson, Tomas Bergh and Dan Hagstedt for all the valuable discussions and all the laughter during the years.

Many thanks to Hotel Sjöström in Gothenburg for offering me such beneficial prices. Your breakfast is amazing.

This work has been financed by SAAB Automobile and the Swedish Energy Agency, which is gratefully acknowledged.

Finally, I would like to thank my lovely family for all their support and always believing in me. My mother for being the best mother one can have and Lisen, the wisest and most beautiful girl I know, for being mine.

Lund, June 2007
Jonas Ottosson

Contents

Chapter 1

Introduction

1.1 Motivation

Hybrid vehicles have attracted tremendous attention during the last few years. This is a consequence of several factors, such as growing environmental concerns, increasing oil prices and a need of oil independency. According to some, we are rapidly approaching the top of the oil era. If this is true, the diminishing availability of crude oil will escalate the already high fossil fuel prices. Many countries, there among Sweden, have declared national actions plans to reduce the oil consumption significantly. The background of the desired reduction in oil use, differ between countries, but the two main concerns are the environmental effects and the wish for independency of oil import. Whatever the concern is, economical, independency or environmental, how does hybrid vehicles fit in this context?

Hybrid vehicles have proven to have significant potential to improve fuel economy without reducing the performance of the vehicle. Keeping or even enhancing, which often is the case, the drivability is an important issue in order to reach customer acceptance. Except for gains in the fuel economy, hybrid vehicles have also demonstrated potential for reducing exhaust emissions. Most hybrid vehicles on the market today, are hybrid electric vehicles (HEV) with an internal combustion engine (ICE) and at least one electrical machine. Toyota was the first major automaker to introduce a commercial vehicle, the Toyota Prius. The commercialization in the recent years has mainly been possible due to advances in the battery and power electronics technologies. The HEVs mainly benefit from the following; down-sizing or "right"-sizing of the engine, still fulfilling the power demanded from the driver, recovering energy during deceleration by operating the electrical machine as a generator, eliminating the fuel consumption originating from engine idling by shutting the ICE off and

operating the ICE more efficiently, since an extra degree of freedom is available to satisfy the power demand.

With this background given, it is clear why almost all car manufactures are developing HEVs today. This thesis is based on experiences from the development of a HEV as a part of a cooperation between SAAB Automobile and Lund University.

1.2 Objectives

Optimization of a rather simple heuristic control strategy, without adding to much complexity. In addition to this, determine the "the degree of optimality" of the heuristic control strategy by comparing it to an optimal control strategy obtained with global optimization. The global solution to the HEV energy management control problem is determined with Dynamic Programming.

Develop and commission an electrically driven rear-axle for a hybrid car, focusing on control and modeling. This includes the development and implementation of a field weakening controller for control of the electrical drive. Furthermore, develop a thermal model of the machine, which will serve as a basis for the development of an over temperature controller.

1.3 Outline of the Thesis

The thesis is divided into two parts, where the first part is devoted to energy management strategies in HEVs and the second part presents the implementation and validation of a electrically driven rear-axle for hybrid car. Chapter 2 introduces different hybrid topologies and gives a short summary of their advantages and disadvantages. Chapter 3 contains models and data for the different components of a reference vehicle. Chapter 4 gives a short introduction to an heuristic energy management strategy, named *Optimal Engine Line Strategy*. The importance of choosing the correct number of gears and the individual gear ratios are discussed. Since the reference vehicle has two electrical machines, the power split between these two are considered. In the end of the chapter the choice of energy management controller parameters, to achieve minimum fuel consumption, are discussed. Chapter 5 is devoted to dynamic programming to obtain an optimal control strategy, which is used as a benchmark for the heuristic control strategy. In Chapter 6 conclusions regarding energy management are given. Chapter 7 introduces

the components of a electrically driven rear-axle, called the rear drive unit (RDU). It also contains a field weakening controller scheme. Chapter 8 presents a simple thermal model of the electrical machine used for the rear-axle. Experimental results are presented to validate the proposed thermal model. In addition to this an over temperature controller is proposed. In Chapter 9, conclusions regarding the RDU are presented. Chapter 10 gives the concluding remarks and a summary of the findings is presented together with suggestions for future work.

1.4 Contributions

The main contributions of the thesis can summarized as follows:

- The choice of control parameters, in order to achieve minimal fuel consumption, for a heuristic control strategy is discussed.
- The importance of modifying standard components, such as the gearbox, to adapt to the hybrid drivetrain is discussed.
- A comparison of two different methods of splitting the electrical power, when two electrical machines are used, is presented.
- An optimal solution to the HEV control problem for a HEV, obtained with Dynamic Programming, with two electrical machines is presented.
- A comparison of the optimal solution to the heuristic control strategy is presented, where the optimal solution serves as benchmark.
- A simple and effective type of field weakening controller, based on measurements, is proposed.
- A thermal model has been developed and validated against measurements.
- An over temperature controller, to prevent the electrical machine from overheating, is proposed.

Part I

Energy Management in Hybrid Electrical Vehicles

Chapter 2

Electrical Hybrid Vehicle Topologies and Modeling

2.1 Hybrid vs. Conventional Vehicle

The first battery powered electric vehicle (EV) was built by Thomas Davenport in 1834. However, it wasn't until the 1970s that the development of EVs really took place. The interest in EVs has its origin in the problems of the internal combustion engine (ICE), such as high fuel consumption, exhaust emissions and the increasing dependency of foreign oil. EVs are considered as an alternative to ICE powered vehicles to reduce these problems. EVs offer high energy efficiency, diversification of energy resources, zero or minimal global exhaust emissions and quiet operation. However, it has two major drawbacks – short driving range [1] and high power requirements if rapid charging should be possible. The energy content in a 100 kg lithium ion battery, which is the type of battery with the highest specific energy on the market today, is only 15 % compared to a normal sized fuel tank. This figure is calculated taking into account the significantly higher mean efficiency of the electric drive system, which is in the vicinity of 80% compared to 20% for the ICE. There is today a tremendous development of traction batteries and the specific energy will most likely increase significantly in the years to come. There is, however, one major obstacle with EVs, and that is the "re-fueling". Assume that there exists a battery with a storage capacity of 100 kWh, which corresponds to a driving range of approximately 500 km. If the battery is to be charged in 6 minutes, i.e. a tenth of an hour, the power needed is 1 MW. This power level is unacceptably high. One solution to the high power requirements for re-fueling and short operating range of the EVs, and the poor efficiency of the ICE powered vehicles is the hybrid vehicle.

There are many different definitions of a hybrid vehicle. In 2003, UN stated the following definition for a hybrid vehicle [2].

"A hybrid vehicle is a vehicle with at least two different energy converters and two different energy storage systems (on-board the vehicle) for the purpose of vehicle propulsion".

The hybrid electric vehicle (HEV), which is a subset of hybrid vehicles, consists of either an internal combustion engine or a fuel cell as the primary energy converter, also called the primary power unit (PPU), and at least one electric machine as the secondary energy converter. The two energy storage systems are consequently some kind of fuel tank and battery or super capacitor.

The basic definition of a hybrid HEVs offers rapid refueling compared to EVs, which have to recharge the traction batteries. This can take several hours, depending on the size of the battery and the charging power. One drawback of HEVs compared to EVs is the loss of the zero emission concept. However, with a significantly large battery it is possible to operate the HEV in an all-electric mode for considerable distances. The all-electric mode could for instance be used in urban areas where exhaust pollutions affects a significant amount of people. The HEVs on the market today has a rather limited driving range in all-electric mode, only up to a few kilometers. It should, however be mentioned that there are a lot of research and development of a type of HEV called plug-in hybrid. The plug-in hybrids are meant to be charged from an ordinary wall outlet and to have an all-electric driving range of about 50 km. This driving range covers a significant amount of the trips for an average car and will consequently decrease the fuel consumption drastically. One drawback with all types of HEVs are the increased cost, which is partly connected to the increased complexity of the vehicle. This might be a barrier for the number of sold HEVs in the world. However, manufacture costs will, according to [3], decrease significantly as production volumes increases.

As was mentioned before, HEVs are a very promising technology for improving fuel economy and reducing emissions. The two most important features of the HEV contributing to a better fuel economy is a more efficient operation of the ICE and regenerative breaking. The more efficient operation of the ICE originates from the possibility to choose the working points of the ICE more freely. This can be done due to the fact that the demanded power

from the driver can be delivered not only by the ICE but also from the electric drive system. When the power demand from the driver is low, the HEV has the possibility to operate the ICE on a higher power, which implies a higher efficiency. The extra energy generated can be stored in the energy buffer for future use. Furthermore, the over all energy efficiency can be significantly improved by operating the electrical machine as a generator during deceleration of the vehicle. Instead of, as in a conventional car, wasting the kinetic energy as heat in the mechanical brakes, the HEVs capture some of this energy. The amount of energy that can be regenerated is limited by the maximum power of the electric drive system and the state of charge (SOC) of the battery. If the electric machine is unable to provide all of the necessary brake torque, the mechanical brakes steps in.

Another benefit from hybridization of a vehicle is a feature called start/stop. This feature saves energy by shutting of the ICE when the vehicle is at standstill. Then when the gas pedal is pushed the ICE automatically starts. If the power of the electric drive is high enough, the vehicle take-off can be done all electric and the ICE can be left off until the power demand is too high for the electric drive or the SOC is low. The ICE, can in a HEV, be downsized and chosen to meet the average power demand. During heavy loads, the electric drive system steps in and assists the ICE. This contributes to a more efficient use of the ICE.

2.2 Hybrid Topologies

HEV:s are traditionally classified into two basic configurations, the series and the parallel hybrid. There also exist configurations, which is a combination of these two basic ones.

Series Hybrid Drivetrain

The development of the series hybrid drivetrain originates from the desire to solve the problem with the short driving range of the EVs. The battery is charged through a generator using a small ICE. A schematic picture of the series hybrid drivetrain is shown in Figure 2.1.

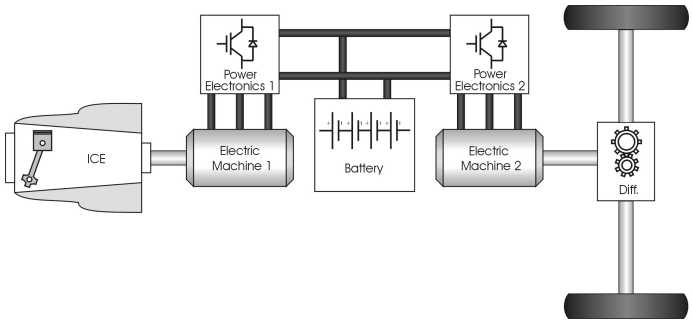

Figure 2.1 Series hybrid drivetrain.

The thermal energy stored in the tank is converted to mechanical energy in the combustion engine. The mechanical energy is then transformed to electric energy in the generator and stored in the electric energy buffer via a power electronic converter. The electric energy is then transformed back to mechanical energy via the electric traction motor and its associated power electronic converter. The advantages and disadvantages of the series hybrid powertrain are summarized in Table 2.1.

Table 2.1 Advantages and disadvantages of the series hybrid drivetrain [4].

Advantages	Disadvantages
Mechanical decoupling of the ICE and wheels. Allows the ICE working point to be chosen for high efficiency.	Requires a large traction motor as it is the only torque source. Has to be designed for peak power.
Simple speed control due to a single torque source connected to the wheels.	The many energy conversion leads to a low overall system efficiency.
Using an electric machine as the only torque source eliminates the need for a multi gear transmission.	Needs two electric machines and two sets of power electronics.
Simple packaging as the ICE and the generator can be mounted separately from the traction motor.	

The series hybrid is not suitable for high way traffic due to the many energy conversions. However, in urban traffic it can be made very efficient with the proper control. In addition, the packaging advantages make the series hybrid drivetrain suitable for heavy vehicles, such as commercial buses and military vehicles.

Parallel Hybrid Drivetrain

The parallel hybrid drivetrain consists of an ICE and at least one electric machine, which are both mechanically connected to the wheels as shown in Figure 2.2.

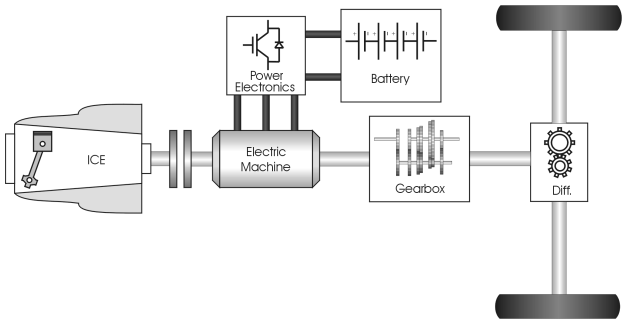

Figure 2.2 Parallel hybrid drivetrain.

The electric motor can be connected to the drivetrain in several different ways and can be located anywhere along the transmission. The mechanical coupling can be a gearbox, a belt or the rotor of the electrical machine being a part of the shaft, which is the case in Figure 2.2. The basic operation of the parallel hybrid is that the speed of the ICE is chosen with the gearbox in order to keep the engine speed within its limits. The electric machine can then be used to add or subtract torque to the engine torque in order to achieve a high ICE efficiency. The electric machine can also be used during regeneration to charge the energy storage. In some configurations, where the ICE can be disengaged from the drivetrain, the vehicle can be run in pure electric mode. The advantages and disadvantages of the parallel hybrid are summarized in Table 2.2 [4].

Table 2.2 Advantages and disadvantages of the parallel hybrid drivetrain.

Advantages	Disadvantages
Both the engine and the motor are connected directly to the wheels, which leads to fewer energy conversions.	The mechanical coupling of the ICE to the wheels leads to a more limited choice of operating points.
Compact configuration and no need for a generator	
Can use a smaller battery pack and a smaller traction motor.	

The major advantage of the parallel hybrid compared to the series hybrid is that the ICE is directly coupled to the wheels. This eliminates the inefficiency of converting mechanical power to electricity and back. Unlike the series hybrids, this makes the parallel hybrid drivetrains suitable for highway traffic. However, the mechanical coupling is also a drawback of the parallel configuration, since the ICE is to some extent forced to follow the power request. This is, however, not a major problem, since a gearbox is normally used and the operating point of the ICE can thereby be varied. The compactness of the parallel hybrid drivetrain and the fact that it can be used both for city- and highway traffic makes it suitable for both small and heavy vehicles.

Series-Parallel Hybrid Drivetrain

The series-parallel hybrid drivetrain, also known as the power split hybrid (PSH), is a configuration intended to combine the advantages of the series and the parallel configuration. The configuration consists of one ICE and two electric machines as seen in Figure 2.3.

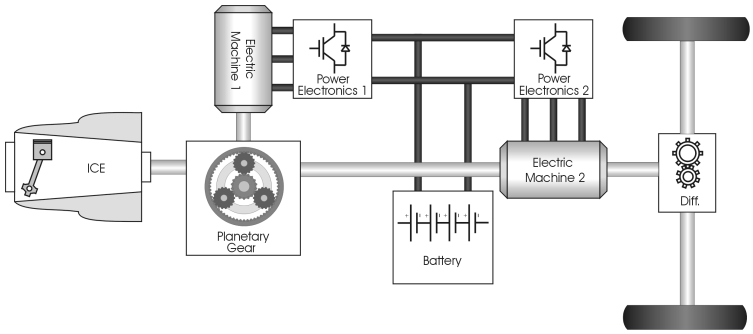

Figure 2.3 Series-parallel hybrid drivetrain.

A planetary gear set is used to connect the electric machines and the ICE. The first electric machine, often referred to as the generator, is connected to the sun wheel, the ICE is connected to the planet carrier and the second electric machine, often referred to as the traction motor, is connected to the ring wheel. The generator is used to adjust the speed of the ICE, while the task of the traction motor is to adjust the torque. Thus, the operating point of the ICE can be continuously varied by the electric machines. The planetary gear, together with the electrical machines, work as a continuously variable transmission (CVT). The difference between a CVT and an ordinary transmission is that the CVT can vary the ratio continuously, while the ordinary transmission has discrete steps for each gear. One drawback with this configuration is that the generator has to be designed to meet the peak torque of the ICE. One other drawback is that, if the generator or the power electronics controlling it malfunctions, the vehicle will not move at all. In the case with the parallel configuration, the vehicle can still be propelled by the ICE.

Chapter 3

Reference Vehicle and Modeling of Vehicle Components

Simulation of hybrid vehicles includes many different kinds of components. Hence, the models of the respective components have to be relatively simple in order to keep simulation times within reasonable limits. However, the simplified models still have to be able to describe the general behavior of their physical counterpart.

3.1 Background

In the spring of 2004 cooperation between SAAB Automobile and Lund University (LU) was started in order to build a hybrid electrical vehicle. The project was given the name "MHD-II-project". The goals of the project can be divided into two main parts; pure technical performance goals and knowledge enhancement goals. The performance goals were stated by SAAB Automoblie and served as input to LU. The performance goals is summarized below

- Fuel consumption reduction > 25%
- Acceleration time, 0 –100 km/h < 8,5s
- Acceleration time, 80 – 120 km/h < 8,0s
- Maximum speed > 200km/h
- Emission levels equal to or lower than today's levels (Miljöklass 1), preferably lower than EURO V.

3.2 Vehicle Configuration

The vehicle model used in this thesis is based on data from a conventional SAAB 9-3. The vehicle configuration can be seen in Figure 3.1.

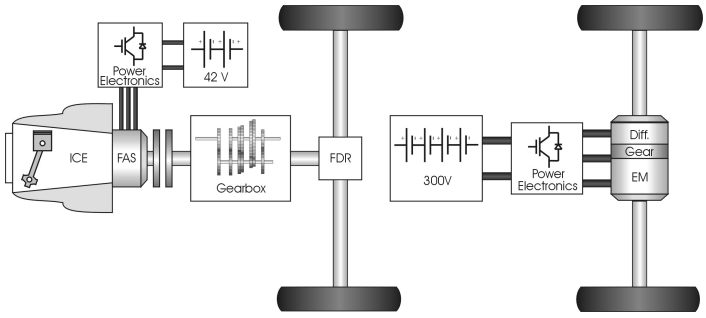

Figure 3.1 Reference vehicle drivetrain configuration.

Data for the different vehicle components are provided by SAAB Automobile and presented in detail in the following sections. The configuration is clearly of the parallel type. It has as its PPU an ICE, which is a four-stroke (4S) spark ignited (SI) engine with four cylinders and a turbo. The vehicle is also equipped with two electrical machines, which are of different sizes and power ratings.

The smaller electrical machine is mounted between the ICE and the gearbox. The machine acts as a replacement for the flywheel and is operated as an alternator/starter. This type of configuration is commonly referred to as a flywheel alternator starter (FAS). The clutch between the FAS and the gearbox is used to disengage the engine during gear shifting and in electrical operation. The FAS is powered by a 42 V battery and its accompanying power electronics. This power electronics is in its turn connected to a DC/DC-converter. This DC/DC converter acts as a bidirectional energy transfer device, i.e. it can transfer energy between the 42 V and the 300 V batteries in both directions. The battery management unit (BMU) keeps track of the state of charge (SOC) of all the individual battery modules of the 300 V battery and redistributes the energy between the modules. This is an important feature for maximizing the lifetime of the traction battery.

The 300V battery powers the second electrical machine, which is mounted

on the rear axle. The electrical machine is one constituent part of what is called the rear drive unit (RDU). This electric machine will be referred to as the RDU throughout the thesis, even though it also consists of a differential and a planetary gear. The planetary gear is required to accomplish a high wheel torque. The gear ratio of the planetary gear, R_{RDU}, is 6,1. In a vehicle with a transverse engine, there is not much room for squeezing in an electrical machine. The power rating of the machine is consequently limited due to the lack of space, since the physical size of the electrical machine is proportional to its power rating. Thus, one simple way to increase the electrical power on-board the vehicle, is to add an electrically driven rear-axle. The benefit of this, except for more installed power, is that the vehicle will be four-wheel driven without the need of a propeller shaft. The RDU and its power electronics are studied more in Part II of the thesis.

3.3 Chassis Model

A vehicle is exposed to many different forces acting in all three dimensions. However, to study different hybrid control strategies only a simple longitudinal model is needed. Thus, vehicle stability will not be considered in this one dimensional model. A vehicle that is moving up a grade is exposed to a resistance force. The change in vehicle speed can, according to Newton's second law of motion, be calculated as

$$m_v \frac{dv}{dt} = F_t - F_r \tag{3.1}$$

where v is the vehicle speed, F_t is the tractive force, F_r is the resistance forces and m_v is the vehicle mass. The resistance force consists of three different parts: tire rolling resistance, aerodynamic drag resistance and the uphill resistance. The total resistance force, F_r, can be expressed as [6]

$$F_r = C_r m_v g \cos(\gamma) + \frac{1}{2}\rho_a C_d A_v v^2 + m_v g \sin(\gamma) \tag{3.2}$$

where C_r is the rolling resistance coefficient, γ is the road angle, ρ_a is the air density, C_d is the aerodynamic drag coefficient, A_v is the vehicle front area and g is the acceleration of gravity . All of the above mentioned vehicle parameters are presented in Table 3.1.

Table 3.1 Vehicle parameters.

Parameter	Value
m_v	1770 kg
C_d	0.297
C_r	0.0118
ρ_a	1.225 kg/m^3
A_v	2.16 m^2
r_w	0.308 m
g	9.82 N/kq

The road angle is set to zero throughout the thesis, which simplifies Equation (3.2) above. The reason for this is that the driving cycles used in the simulations, see Appendix C, do not contain any information about the road inclination.

3.4 Internal Combustion Engine

The internal combustion engine is a very complex device and consequently some kind of simplified model has to be used. The efficiency of the ICE can in stationary operation be measured for the whole range of possible operating points and stored as an efficiency map. This is often referred to as a "quasi-static" assumption, where the ICE fuel consumption at any instant in time is a static function of engine speed and engine torque. It should be noted that the "quasi-static"-assumption is only valid for normal operation temperatures [5]. Figure 3.2 shows the efficiency map for the ICE used in this thesis. The ICE is a SI-engine with four cylinder and its basic data is presented in Table 3.2.

Table 3.2 ICE specifications.

Parameter	Value
Displacement:	2.0 liter
Max. power:	128 kW
Max. power speed:	5500 rpm
Max. torque:	265 Nm
Max. torque speed:	2500 – 3500 rpm

In dynamic operation of the ICE there will be physical phenomena causing the transient efficiency diverging from the stationary map. One simplification

that is often used is to assume that ICE is operated in stationary operation, which can be considered true if the dynamics of the ICE is limited to around 1 s [7]. Slowing down the dynamics of the ICE is mainly desirable in order to decrease the emissions coupled to the transient operation. This can, in a HEV, be achieved by letting the electrical machine deal with the power transients.

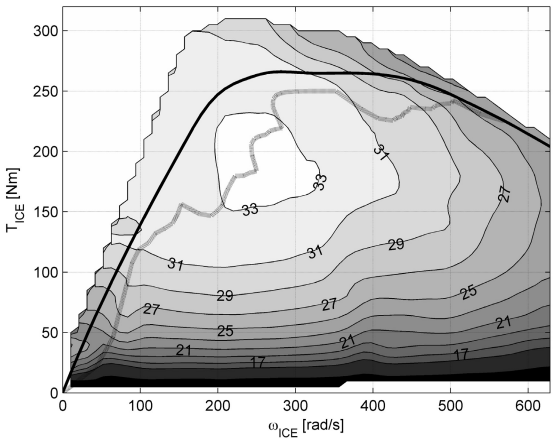

Figure 3.2 ICE efficiency as a function of engine speed and torque. The black solid line represents the maximum engine torque as a function of speed and the dashed line represent the maximum efficiency for all different power levels..

Figure 3.2 shows, as has been mentioned before, the ICE efficiency for different combinations of ICE load torques and speeds. Also shown in the figure is the maximum torque as a function of vehicle speed. The efficiency varies significantly with the current operating point. As the torque is increased for a fixed engine speed, the efficiency increases. That is mainly due to the throttle being more open, which results in a higher inlet pressure and consequently lower pumping losses. A wide-open throttle indicates high power and the percentage of the losses to the total power becomes small.

3.5 Electrical Machines

The two electrical machines used in the hybrid vehicle are of the type interior permanent magnet synchronous machines (IPMSM). The reason for using

this type of machine is that it has high efficiency and high power density, requires low maintenance and is relatively easy to control [8]. All this together makes the PMSM a competitive choice when it comes to tractive applications. However, it has its drawbacks, such as relatively low efficiency for high speeds, due to the demagnetizing current needed for field weakening, and having expensive permanent magnets as the source of magnetic flux. Another drawback is that it has a low speed ratio, i.e. low ratio between the maximum speed and the base speed, which is disadvantageous for vehicle acceleration compared to electrical machine power. Data for the two electric machines are presented in Table 3.3.

Table 3.3 Electrical machine specifications.

	FAS	**RDU**
Parameter	**Value**	**Value**
Continuous power	7 kW	18 kW
Continuous torque	40 Nm	50 Nm
Intermittent power	12 kW	36 kW
Intermittent torque	120 Nm	90 Nm
Pole number	32	8
Base speed	1700 rpm	4100 rpm
Rated voltage	42 V	300 V

The electrical machines are modeled as efficiency maps with torque and speed as input and efficiency as output. Figure 3.3 shows the efficiency maps for the two electrical machines both for motor and generator operation. It also shows the maximum and minimum torque as functions of speed.

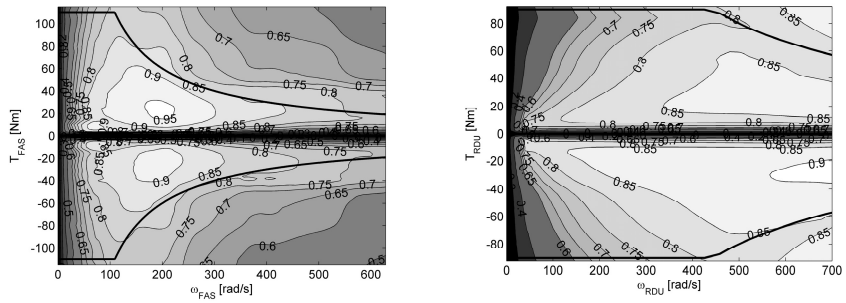

Figure 3.3 Electrical machine efficiency for the FAS (left) and RDU (right).

Figure 3.3 shows that the efficiency differs significantly depending on operating point. Copper losses are dominant for low speeds and are highly dependent on the torque level. As speed increases, the core losses increase and eventually become predominant at high speeds. The copper losses also increase at high speeds due to the increase in demagnetizing current needed for flux weakening. It should be mentioned that the losses of the power electronic converter connected to the FAS is included in the efficiency map presented in Figure 3.3.

3.6 Battery

The vehicle is equipped with two different batteries, one low voltage (42 V) and one high voltage (300 V) battery connected to the FAS and the RDU, respectively. The low voltage battery will not be included in the simulation model. Hence, it will be assumed that the FAS is connected to the high voltage battery. This can be considered a reasonable simplification since the purpose of the simulation model is to study overall energy management strategies rather than the utilization of the batteries. Another justification is that it is normally desirable to have as few voltage levels in the vehicle as possible.

The purpose of the battery in a hybrid vehicle is to store and supply energy. There exists many different types of batteries. However, there are only a few types that are suitable for tractive applications. Four different parameters are important to consider when a battery is to be chosen, i.e. the energy density, power density, cycle life and cost. The traction battery used in the hybrid vehicle studied here is a Nickel-Metal Hydride (NiMH) battery, which is a battery type that is a good compromise between these four parameters. The basic data for the battery is given in Table 3.4.

Table 3.4 Traction battery specification.

Parameter	Value
Cell voltage	1,2 V
Series cell resistance (25°C)	2,1 mΩ
Number of cells in series	252
Rated voltage	302 V
Power capacity	30 kW
Energy capacity	1.8 kWh
Weight	55 kg (80 kg)

A simple simulation model of the battery, based on the data presented in Table 3.4 and additional measurements, is derived in Appendix A. The main result is an efficiency map, presented in Figure 3.4 with the terminal power, P_{term}, and state of charge (SOC) as inputs.

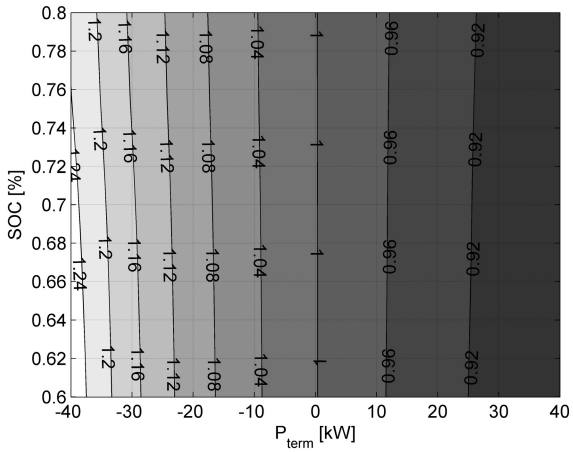

Figure 3.4 Battery efficiency as a function of terminal power, P_{term}, and SOC.

Figure 3.4 shows that the efficiency is highly dependent on the terminal power, whereas for the SOC the dependency is almost negligible. The difference in efficiency between 60% and 80% SOC is only 2%. Hence, the battery efficiency will be considered to only be a function of P_{term}. The variation of the efficiency, for all SOC levels are henceforth assumed to be equal to the efficiency variation obtained with the SOC equal to 70%.

3.7 Gearbox

The main objective of the gearbox, irrespective of the type of transmission, is to keep the engine speed and torque within its operating area regardless of the speed and torque requirements at the wheels. This adaptation of speed is accomplished in different ways for a manual and an automatic transmission. The manual transmission is based on engaging various gear combinations to the output shaft in order to achieve different gear ratios. The automatic gearbox however, uses bands, clutches and a torque converter to achieve the same gear ratios [7]. The torque converter can increase the torque from the

engine about two times when the engine is turning much faster than the transmission. Hence, this torque boost normally occurs during take-off. The major disadvantage of the automatic transmission is its relatively low efficiency compared to a manual transmission. The low efficiency is a consequence of two things, slip in the torque converter and pumping losses originating from an oil pump in the gearbox. Therefore, an automatic transmission seldom has an efficiency over 90 %, compared to a manual transmission, which normally has an efficiency over 96%.

The gearbox in the reference vehicle is a 6-speed automatic transmission. However, the gearbox will be modeled as a robotized manual transmission, which will result in a loss of the torque boosting effect from the torque converter. The efficiency of the modeled transmission is set to a fixed value of 90%, to correspond to the automatic transmission. The transmission gear ratios and the final drive ratio (FDR) are given in Table 3.5.

Table 3.5 Transmission gear ratios and final drive ratio.

Gear	Ratio
1:st	3.79
2:nd	2.04
3:rd	1.33
4:th	0.95
5:th	0.76
6:th	0.62
Reverse	3.57
FDR	3.54

The optimal number of gears and their individual gear ratio will be discussed in Chapter 4.2. It will be shown that it is of vital importance for the proposed energy management strategy that the gear ratios are chosen properly in order to achieve minimal fuel consumption.

3.8 Power Electronics

Power electronics are an important part of a hybrid vehicle since it controls the speed and the torque of the electrical machines. It also serves as an interface between the DC-side of the battery and the AC-side of the electrical machine. This type of power electronics, where there is a DC- and an AC-side and the power flow is bidirectional, is usually referred to as switch-mode

DC-to-AC converter.

As for all of the other components described in this chapter, the power electronics prove to have losses. The losses mainly originate from the switchings associated with the pulse width modulation (PWM). During commutations, when the power electronic switch changes state from on to off and vice versa, there is a short period of time where the switching device is exposed to both high voltage and high current at the same time. This results in high power dissipation in the switch device during turn-on and turn-off. The switching devices also have conduction losses due to a small voltage drop in the on-state. So the losses depend on many parameters, current, voltage, switching times and switching frequency to mention a few [9]. However, the mean efficiency of the power electronic converters are high and setting the efficiency to a fixed value of 97% is a reasonable simplification [7].

Hence, the efficiency for the power electronic converter connected to the RDU is set to 97%. The efficiency for the converter connected to the FAS is included in the efficiency map presented in Figure 3.3.

3.9 Simulation Model

All of the vehicle components, such as the ICE, FAS, RDU, transmission and battery, described in the preceding sections have been implemented in Simulink/Matlab, together with road and driver models. Figure 3.5 shows the top level of the simulation model.

The simulation model also contains to control blocks, the power flow controller and brake controller. The power flow block handles the demanded torque from the driver and manages the power split for the three different torque sources, i.e. the ICE, FAS and RDU. This block also contains a SOC controller, which keeps the SOC within pre-defined limits. The brake controller block controls the use of the mechanical brakes. The mechanical brakes are only used if the electrical machines are unable to deliver the braking force commanded by the driver or if the battery is unable to store the breaking energy.

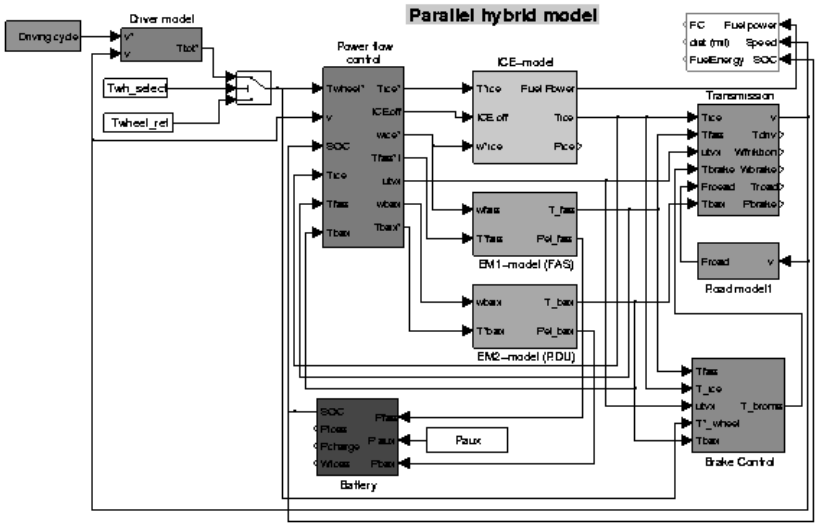

Figure 3.5 Top level of the simulation model for the reference vehicle.

Chapter 4

Optimal Operating Line Strategy

An HEV has, apart from the ICE, at least one additional source of power available for vehicle propulsion. The control of these power sources is managed by an energy management controller and its associated energy control strategy. The control strategy has several different objectives, where the primary ones usually aim to minimize the fuel consumption and emissions. The control objectives are achieved by instantaneous management of the power split between the power sources. This power split is crucial for the overall performance of the HEV system. Apart from achieving a high fuel economy and minimizing the emissions, the strategy must maintain the driveability or preferably enhance it. One peculiarity with this type of control problem is that the control actions are local in time, whereas the control objectives, such as fuel consumption, emissions per distance and SOC of the battery, are integral [10]. Many different control strategies have been proposed and they can be classified into two different classes. The first one is real-time algorithms that can be used for real time control. This first class of control algorithms is normally developed using two different types of techniques, parameter-tuning techniques such as rules ([11]) or fuzzy logic ([12]) and static optimization techniques ([10],[13]). The static optimization method is commonly based on translating the instantaneous use of electrical energy into fuel energy in order to calculate the overall fuel cost. The second class of control algorithms is global optimization techniques that rely on the driving cycle being known in advance. This second class is often used as a benchmark and for evaluation of the first class of algorithms. These control techniques are horizon based and two different techniques are used, such as dynamic programming (DP) ([14],[15]) and optimal control theory ([16]).

4.1 Optimal Engine Operating Line Strategy

Control strategies based on parameter-tuning techniques, often referred to as heuristic control strategies, are simple, easy-to-use and robust. Heuristic control strategies are also significantly less computational burdensome, compared to the horizon based strategies. One example of a heuristic control strategy is the *load following* strategy presented in [18], here referred to as the optimal operating line strategy. A short description of the basic idea behind the strategy will be presented in this chapter. The term *load following* referrers to the operation of the PPU, where its task is to follow the drivers power demand. However, the dynamics of the PPU are limited in order to avoid rapid transients, which result in high emission levels [18]. To maintain the driveability, the electrical machines steps in and takes care of the rapid transient. Hence, the requested power is consequently split between the ICE and the electrical machines, and the PPU is in reality only partially load following. The statement of the instantaneous power split between the ICE and the electrical machines can be summarized in the following equation

$$P_{wh}^{*}(t) = P_{ICE}(t) + P_{EM}(t) \tag{4.1}$$

where P^{*}_{wh} is the power demand from the driver and P_{ICE} and P_{EM} is the ICE power and the total electrical machine power, respectively. In order to slow down the dynamics of the ICE a simple low pass filter, with the time constant τ_{ICE}, is used. The time constant τ_{ICE} is a design parameter, that affects the utilization of the ICE and consequently the battery, since Equation (4.1) must hold. How τ_{ICE} should be chosen, in order to achieve the best fuel consumption will be discussed in Chapter 4.4. The power level of the ICE can be achieved by several different combinations of engine torque and speed. However, for every power level, there is one combination of torque and speed that gives the highest ICE efficiency. The basic function of the strategy is to chose operating points along this line to achieve a high mean ICE efficiency. This is were the name, optimal engine operating line strategy, originates from. These combinations are represented as a line in Figure 3.2. These torque and speed combinations are pre-computed and stored in a look-up table (LUT). Equation (4.2) below shows how the torque and speed reference for the ICE is computed.

$$T^*_{ICE}(t) = LUT_{ICE}\left(P^*_{ICE}(t)\right)$$
$$\omega^*_{ICE}(t) = \frac{P^*_{ICE}(t)}{T^*_{ICE}(t)} \tag{4.2}$$

where T^*_{ICE} and ω^*_{ICE} is the ICE torque and speed reference, respectively. LUT_{ICE} is the pre-computed look-up table converting the ICE power reference into a torque reference. A gearbox is used to set the engine speed. The reference speed for the ICE is known from Equation (4.2) and the vehicle speed is known from the driving cycle, the ideal ratio can be computed according to Equation (4.3).

$$R_{ideal}(t) = \frac{\omega^*_{ICE}(t)}{\omega_{wh}(t)} \tag{4.3}$$

R_{ideal} is the ideal gear ratio and ω_{wh}.is the wheel speed. The gear with the ratio closest to the ideal ratio is chosen. The outcome of choosing gear in this manner is that the ICE operating points will be chosen close to the optimal engine operating line. Since the gearbox only has a discrete set of gear ratios, the ideal ratio and the ratio of the chosen gear will differ. The choice of gear and new operating point can be computed as

$$i(t) = \min_i\left(\left|R_i(t) - R_{ideal}(t)\right|\right)$$
$$T^*_{ICE_{new}}(t) = \frac{T^*_{wh}(t)}{R_i(t)} \tag{4.4}$$
$$\omega^*_{ICE_{new}}(t) = \omega^*_{ICE}(t)R_i(t)$$

The parameter i is the number of the chosen gear and R_i is its associated gear ratio. T^*_{ICEnew} and ω^*_{ICEnew} is the torque and speed of the engine after selecting a suitable gear. The difference of the optimal and the achieved operating point inherited by the discrete set of gear ratios, implies that the overall performance of the control strategy is dependent, not only on the individual gear ratios, but also on the number of gears. This issue will be discussed further in Chapter 4.2.

The mean efficiency of the ICE can be improved by simply not allowing the ICE to be operated if the efficiency is to low. This is typically the case in urban driving where the power requirements are low. However, the power demand must still be met and the electrical machines will have to supply the tractive power needed. This is summarized in the following equation.

$$\begin{cases} P^*_{ICE}(t) = 0 \\ P^*_{EM}(t) = P^*_{wh}(t) \end{cases}, \eta_{ICE}(T^*_{ICE_{new}}(t), \omega^*_{ICE_{new}}(t)) < \eta_{ICE_{off}} \quad (4.5)$$

The efficiency level where the ICE should be turned off, η_{ICEoff}, is a design parameter. The choice of this level will be discussed in Chapter 4.4. Hence, the electrical machines are used both for relieving the ICE from rapid transients as well as low efficiency operation. They are also be used to support the ICE during heavy accelerations and to regenerate energy during deceleration of the vehicle. In addition to the power split between the ICE and electrical machines, the split between the front and rear electrical machines has to be considered. This can be done in different ways and will be discussed in Chapter 4.3.

Extensive use of the electrical machines will result in a depletion of the battery. This is avoided by adding a controller that keeps the SOC of the battery close to a reference value. The reference value for the SOC is here set to 70%, which allows the battery to be charged during decelerations of the vehicle and discharged without reaching to low charge levels. The SOC-controller is implemented as a simple P-controller with the gain k_{SOC}. It should be pointed out, that this type of SOC control is very simple and more sophisticated ones have been presented in the literature [19], [20]. The power used to charge the battery has to be produced by the ICE. Hence, the ICE has to produce the tractive power as well as account for the SOC charging power, yielding the following relation for the ICE power

$$P_{ICE}(t) = \frac{1}{1 + p\tau_{ICE}} \left(P^*_{wh}(t) + k_{SOC} \left(SOC^* - SOC(t) \right) \right) \quad (4.6)$$

where p is the differential operator. The relation for the electrical machine power is given by combining Equation (4.1) and Equation (4.6).

$$P_{EM}(t) = \frac{p\tau_{ICE}}{1+p\tau_{ICE}}\left(P_{wh}^{*}(t) - \frac{k_{SOC}}{p\tau_{ICE}}\left(SOC^{*} - SOC(t)\right)\right) \quad (4.7)$$

The SOC of the battery can be computed as the time integral of the power either charging or discharging the battery, see Appendix A for a complete derivation of the battery model. This statement together with Equation (4.7) results in the following equation for the dynamics of the SOC

$$SOC(t) = \frac{\tau_{ICE}}{1+p\tau_{ICE}}\left(\frac{k_{SOC}}{\tau_{ICE}p}\left(SOC^{*} - SOC(t)\right) - P_{wh}^{*}(t)\right) \quad (4.8)$$

In order for the control loop to be stable, the open loop transfer function has to be stable. This is achieved by correctly choosing k_{SOC} with respect to τ_{ICE}. Depending on the desired relative damping of the control loop, k_{SOC} should be chosen according to

$$k_{SOC} = \frac{W_{bat}}{4\varsigma^{2}\eta_{bat}\eta_{EM}^{-sign(P_{EM})}\tau_{ICE}} \quad (4.9)$$

where W_{bat} is the specific energy of the battery, η_{bat} is the efficiency of the battery, η_{EM} is the efficiency of the electrical machine and ζ is the relative damping of the open loop transfer function. A complete derivation of k_{SOC} is carried out in Appendix B. The choice of τ_{ICE} and the relative damping will be further investigated in Chapter 4.4.

4.2 Number of Gears and Gear Ratios

The importance of using the correct number of gears as well as the correct gear ratios was mentioned in the previous chapter and will here be further discussed. Since low costs are of great importance for car manufactures, it is not an inconceivable guess that they will use standard components, developed for conventional cars, in their hybrid vehicles. One example of this is to, without any modifications, use a standard gearbox in a hybrid application.

Two simulations of the vehicle described in Chapter 3, with the gearbox changed to a 5-speed gearbox, has been carried out. Figure 4.1 shows the ICE working points for a standard 5-speed gearbox and for a 5-speed gearbox with

the gear ratios optimized for minimal fuel consumption. The optimization procedure has been carried out as proposed by [17].

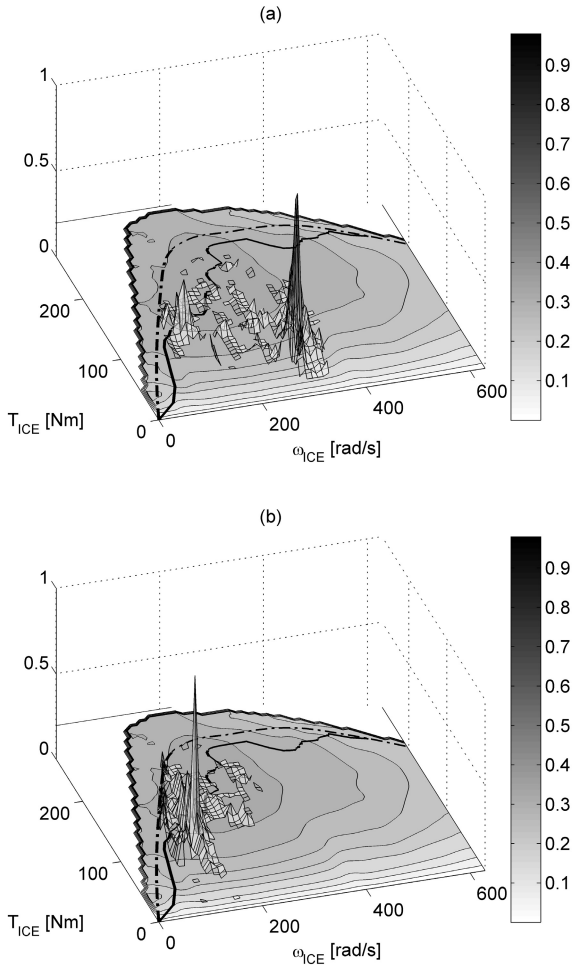

Figure 4.1 Operation of the ICE for a 5-speed gearbox of standard type (a) and of optimized type (b).

Figure 4.1(a) shows that the ICE working points are not concentrated around the optimal engine operating line. Thus, one of the basic ideas behind the

control strategy is not fulfilled and the control objective, high fuel economy, is consequently not reached. The result of the optimization can clearly be seen in Figure 4.1(b), where the operating points are moved closer to the optimal operating line. The fuel consumption is reduced from 0.669 l/10km to 0.580 l/10km for the combined driving cycle, see Appendix C. This corresponds to a decrease of 13%. This is a significant reduction, showing that care should be taken when standard components are used.

The optimization algorithm used to derive the optimal gear ratios for the 5-speed gearbox has also been used to optimize the 6-speed gearbox presented in Table 3.5. The optimization method is based on a Matlab function called *fminsearch*, which is a part of the Optimization toolbox. This routine finds the minimum of an unconstrained nonlinear multivariable function, using a derivative-free method. However, the routine does not guarantee that a global minimum is obtained. Thus, to minimize the probability of ending up in local minimum, several different initial guesses have been tested. All of the initial guesses have ended up in the same values for the optimized gear ratios, which indicates that a global minimum has been found. The result of applying the optimization algorithm to the gear ratios is presented in Table 4.1. It should be pointed out that the FDR is included in the presented values.

Table 4.1 Gear ratios and fuel consumption for standard and optimized 5- and 6-speed gearbox. The FDR is included in the presented gear ratios.

	Gear number						**Fuel consumptiom [l/10km]**
	1	**2**	**3**	**4**	**5**	**6**	
Standard 5-speed gearbox	15.6	8.5	5.2	4.0	3.2	X	0.669
Optimized 5-speed gearbox	17.2	5.9	4.7	2.6	1.5	X	0.580
Standard 6-speed gearbox	13.4	7.2	4.7	3.4	2.7	2.2	0.596
Optimized 6-speed gearbox	17.8	8.3	5.6	3.4	2.1	1.3	0.563

The decrease in fuel consumption for the 6-speed gearbox is not as evident as for the 5-speed gearbox, the decrease in this case is only 6%. The reason for this is mainly due to the 6-speed gearbox having a lower gear ratio for the highest gear, resulting in operating points, during the highway part of the driving cycle, closer to the optimal operating line.

The importance of having the correct gear ratios has been discussed and one solution to achieve almost perfect following of the optimal operating line is to use a continuously variable transmission (CVT). Since a CVT has, between its highest and lowest ratio, an infinite number of gear ratios, the obtained ratio would be equal to the ideal ratio, i.e. the reference ratio set by the control strategy. There are however two drawbacks of the CVT. The first one is that the torque handling capability is limited by the belt or chain used in the construction. Hence, the uses of CVTs are limited to low powered vehicles. The second one is the inability of quick gear changes. One way to approach the advantages of the CVT and at the same time avoid its drawbacks, is to use an automatic transmission with a high a number of gears. The simulations shows that the gain in fuel consumption, when increasing the number of gears from 5 to 6 is relatively small, under the assumption that the gear ratios have been optimized. Hence, there is little to gain from using a CVT or numerous gears, in the cause of minimizing the fuel consumption.

It has been shown that the gear ratios can be chosen to achieve low fuel consumption. However, this is not the only factor that should be considered. Another important factor is the drivability, which probably is equally, if not more, important from a costumer point of view. Figure 4.2(a) shows the relative change in acceleration for a conventional vehicle similar to the reference vehicle, when the standard ratios for the 6-speed gearbox are optimized. It can be seen that the acceleration performance is significantly decreased for the fifth and sixth gear. This would not be acceptable in a commercial vehicle.

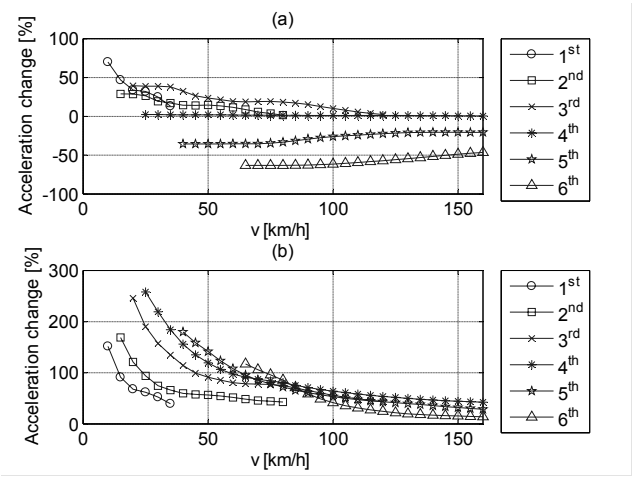

Figure 4.2 Relative acceleration change when the gear ratios of the 6-speed gearbox is changed from the standard values to the optimized ones for conventional vehicle (a) and hybrid vehicle (b), respectively.

The relative change of the acceleration for the conventional vehicle compared to the hybrid reference vehicle, with optimized gear ratios, is shown in Figure 4.2(b). The figure shows that, despite the lower gear ratios for the higher gears, the hybrid vehicle has better acceleration performance for all gears. Hence, the lower gear ratios are compensated by the additional torque from the electrical machines. The drivability is not just kept it is significantly improved. Table 4.2 shows, in addition to the results presented in Figure 4.2, the acceleration performance from 0-100 km/h and 80-120 km/h.

Table 4.2 Acceleration times for 0-100km/h, 80-120km/h and 80-120km/h only using the 5th gear.

	Acc. time, 0-100km/h [s]	**Acc. time, 80-120km/h [s]**	**Acc. time, 80-120km/h (5th gear) [s]**
6-speed standard	7.5	4.6	5.6
6-speed optimized	7.8	4.9	6.8

The results show that the acceleration goals presented in Chapter 3.1 are accomplished, with both the standard and the optimized gearbox. It has been assumed that a gearshift takes 650ms.

4.3 Power Split Between Front and Rear Electrical Machine

The main task of the control strategy is, as has been mentioned before, to determine the optimal power split between the ICE and the electrical machines in order to achieve high fuel economy. Since the reference vehicle has two electrical machines, a split between these two has to be considered.

One way is to split the total requested electrical machine torque between the machines with respect to the machines instantaneous torque capability [18]. This strategy will henceforth be referred to as the available torque strategy. Equation (4.10) describes how the torque split is made.

$$\begin{aligned} T_{FAS}^{*}(\omega_{wh}, R_i) &= \frac{T_{EM}^{*}}{R_i} \frac{T_{FAS_{\max}}(\omega_{wh}, R_i) R_i}{T_{FAS_{\max}}(\omega_{wh}, R_i) R_i + T_{RDU_{\max}}(\omega_{wh}, R_{RDU}) R_{RDU}} \\ T_{RDU}^{*}(\omega_{wh}, R_i) &= \frac{T_{EM}^{*}}{R_{RDU}} \frac{T_{RDU_{\max}}(\omega_{wh}, R_i) R_{RDU}}{T_{FAS_{\max}}(\omega_{wh}, R_i) R_i + T_{RDU_{\max}}(\omega_{wh}, R_{RDU}) R_{RDU}} \end{aligned} \tag{4.10}$$

T_{FAS}^{*} and T_{RDU}^{*} are the reference torques for the FAS and the RDU, respectively. T_{FASmax} and T_{RDUmax} are the respective maximum torques according to Figure 2.1. The instantaneous electrical machine torque is hence a scaled version of the total electrical machine torque reference. The scaling is done by considering each machines torque capability compared to the total available electrical machine torque. The drawback of this strategy is that the electrical torque is always split between the machines. If the torque were low, it would be a better strategy to let one of the machines handle the torque request, instead of imposing both machines to produce a part of the torque. One way to avoid this problem is to pre-compute the best power split in advance, and store the result in a look-up table. This can be done by considering all possible total electrical machine torques and electrical machine speeds and store the power split that generates the highest total electrical machine efficiency. This strategy will in the following be referred to as the pre-computed strategy. The total efficiency, n_{EMtot}, can be expressed as

$$\eta_{EM_{tot}} = \frac{P_{FAS} + P_{RDU}}{\frac{P_{FAS}}{n_{FAS}} + \frac{P_{RDU}}{n_{RDU}}} \quad (motor)$$
$$\eta_{EM_{tot}} = \frac{P_{FAS} n_{FAS} + P_{RDU} n_{FAS}}{P_{FAS} + P_{RDU}} \quad (generator) \tag{4.11}$$

where P_{FAS} and P_{RDU} is the power for the FAS and RDU, respectively. The efficiencies of the respective machine is denoted n_{FAS} and n_{RDU}. In order to study how the torque is split between the two machines, the term power split ratio (PSR) is used. The PSR is defined as the ratio between the FAS power and the total requested electrical machine power, denoted P^*_{EM}.

$$PSR = \frac{P_{FAS}}{P^*_{EM}} \tag{4.12}$$

Three different modes can be distinguished, only the FAS is used (PSR=1), only the RDU is used (PSR=0) and both of the machines are used (0<PSR<1). Figure 4.3 shows the PSR, for the two power split methods, as a function of the total requested electrical machine torque, T^*_{EM} for the US06 driving cycle.

While the available torque strategy always operates in the power split mode, the pre-computed strategy operates in all three modes, which can be seen in Figure 4.3. The mean efficiencies for the FAS and the RDU, during the combined driving cycle, have by using the pre-computed strategy, increased from 65% to 74% and from 62% to 70%, respectively. The result of operating the electrical machines more efficiently is a reduction in the fuel consumption of about 4%. However, it should be pointed out that no consideration has been taken to the vehicle stability. The power split of the electrical machines would in a real vehicle be subordinated the stability control system. Hence, the power split will be overruled by the stability control system in some driving situations.

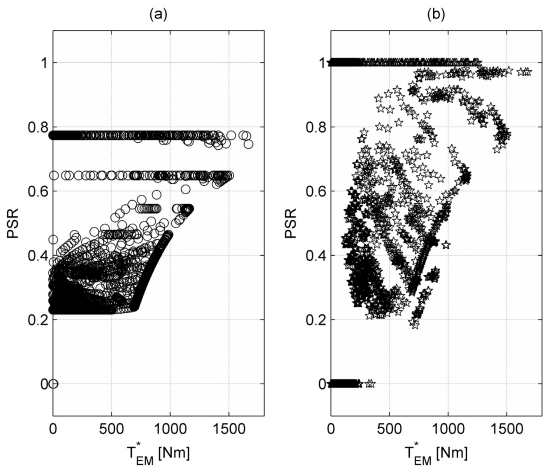

Figure 4.3 PSR for the available torque strategy (a) and the pre-computed strategy (b) as a function of total requested electrical machine torque..

4.4 Tuning of Control Parameters

The optimal engine operating line strategy has three control parameters, τ_{ICE}, k_{SOC} and η_{ICEoff}, which have to be determined in order for the control strategy to work properly. The parameters can be given a value by intuition, but has to be optimized in order to achieve the best possible fuel economy. In Chapter 4.1, it was mentioned that τ_{ICE}, slows down the dynamics of the ICE, which results in lower emission levels. A good starting point for this parameter is 1 s. The charging gain is then chosen according to Equation (4.9), with the relative damping set to one. This results in none oscillatory poles, for the SOC control loop. The last parameter is η_{ICEoff}, which determines at what efficiency level the ICE should be turned off. A high value will result in high stress and high SOC deviations for the battery, where as a low value will result in a lower average efficiency for the ICE. By studying the efficiency map for the ICE, see Figure 3.2, a value of 29 % can be assumed to be a good compromise. The control parameters will all have an effect on the fuel consumption, and the influence of each parameter will be discussed in the following sections. However, by only studying the influence of each parameter separately will lead to a suboptimal solution. Hence, the last section will be devoted to the search of a global optimal solution.

It should be pointed out that, any difference in the final SOC at the end of the driving cycle from the reference value of 70%, has been compensated for. The deviation in the SOC is treated as an equivalent fuel consumption. A positive SOC deviation is seen as fuel consumption reduction since the vehicle could be run in electric mode on the excess battery charge, instead of on the ICE . For the case with a negative SOC deviation, the equivalent fuel consumption is defined as the extra fuel consumption that will be required to recharge the battery via the ICE. The equivalent fuel consumption is added to the fuel consumption obtained over the given cycle and is computed according to Equation (4.13) below

$$\Delta fc = \frac{\left(SOC_{final} - SOC^{*}\right)W_{batt}}{100\eta_{ICEmean}} \tag{4.13}$$

where Δfc is the equivalent fuel consumption, $\eta_{ICEmean}$ is the mean ICE efficiency over the driving cycle, SOC_{final} is the final SOC, W_{batt} is the energy of the battery and SOC^{*} is the SOC reference. To further compensate for SOC deviations, the driving cycles has been run twice in a row. A consequence of this, is that the energy coupled to the SOC deviation will be relative small to the fuel energy used over the cycle. These two methods for compensating for SOC deviations in the end of the cycle has been used through out the thesis.

SOC Controller Gain

The influence of k_{SOC} on fuel consumption has been studied by carrying out several simulations. Two different driving cycles where used in the simulations. The NEDC, which is an urban driving cycle, and US06, which is a highway driving cycle. With τ_{ICE} and ζ equal to one, k_{SOC}, is according to Equation (4.9), equal to 16200. This value is the nominal value for the simulations and will be referred to as k_{SOCnom}. The different values of k_{SOC} were then computed by multipliying k_{SOCnom} with a scaling factor, κ. The values of κ is presented in Table 4.3, together with the associated relative damping.

The effect of changing the SOC controller gain, for the two driving cycles is presented in Figure 4.4. The figure shows the relative change in fuel consumption with regard to the fuel consumption obtained with k_{SOC} equal to k_{SOCnom}. The figure also shows the drift of the SOC. The drift is presented as the mean value of the absolute difference of the instantaneous SOC and the reference value of 70%, taken over the whole driving cycle. It should be

pointed out that η_{ICEoff} and τ_{ICE} was chosen to 29% and 1s, respectively.

Table 4.3 Values for the scaling factor, κ, SOC controller gain, kSOC, and relative damping, ζ, used in the simulations.

κ	$\mathbf{k}_{soc}$	ζ
10	162000	0.32
5	8100	0.45
1	16200	1.00
1/5	3240	2.23
1/10	1620	3.16
1/20	810	4.47
1/30	540	5.48
1/40	405	6.32
1/50	324	7.07
1/70	231	8.37
1/90	180	9.49
1/110	147	10.49
1/150	108	12.25

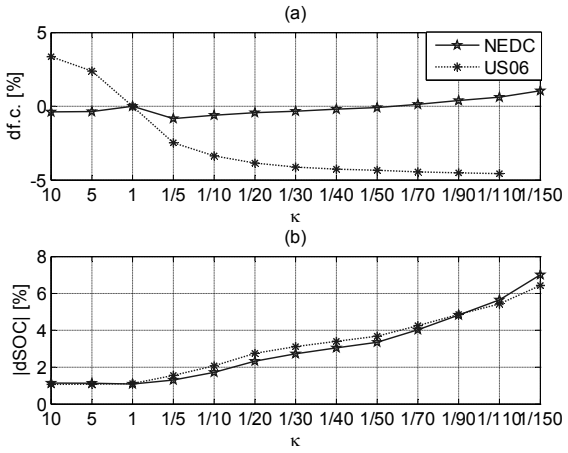

Figure 4.4 Relative change in fuel consumption (a), with regard to the fuel consumption obtained with k_{SOC} equal to k_{SOCnom}. Mean SOC deviation (b) with respect to the reference value of 70 %..

Figure 4.4(a) shows that the fuel consumption varies significantly with the choice of k_{SOC}. An increase in the charging gain with a factor 10, relative to a decrease of 1/50, increases the fuel consumption with approximately 8% for the US06 driving cycle. The reason for this is that, for high charging gains, the ICE almost immediately tries to compensate for a deviation in the SOC. This result in frequent turn-ons and turn offs of the ICE, which results in a lower mean efficiency. An increase in the charging gain also results in higher losses in the electrical path, due to less efficient operating points for the electrical machines. Figure 4.5 shows the relative change in ICE mean efficiency and total loss in the electrical path for both the US06 and NEDC cycle.

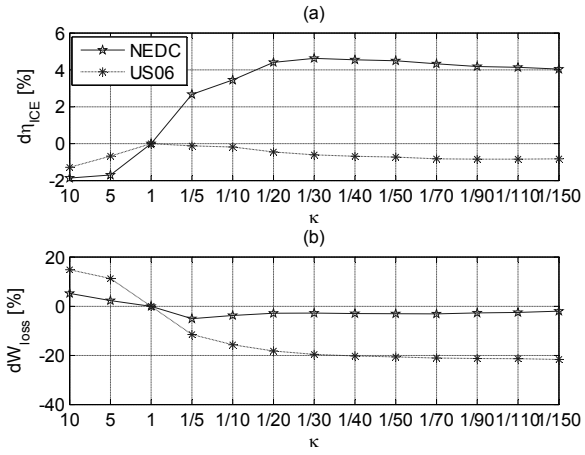

Figure 4.5 Relative change in ICE mean efficiency (a) and relative total energy loss in the electrical path (b), with regard to the mean efficiency and total loss obtained with k_{SOC} equal to k_{SOCnom}.

The decrease in mean efficiency for the ICE is even more evident for the NEDC cycle. However, since this cycle is considerably less demanding than the US06, the ICE is shut off most of the time. Thus, an increase in the mean ICE efficiency will have a negligible effect on the fuel consumption for this cycle.

The results from the simulations also show that the deviation of the SOC increases as k_{SOC} is decreased, see Figure 4.4(b). This is obvious since a lower

gain implies a lower bandwidth of the SOC control loop. As k_{SOC} is decreased, the SOC deviation can reach unacceptable limits, which results in a shorter lifetime of the battery. A reasonable limit for the SOC deviation is assumed to be 15%. The US06 driving cycle exceeds this limit for the lowest scaling factor, whereas the limit is never reached for the NEDC cycle.

ICE Efficiency Turn-Off Level

The ICE is turned off for low efficiencies in order to increase its overall mean efficiency. When the ICE is turned off, the electrical machines have to supply the power request from the driver. However, if the electrical machines are unable to supply the demanded tractive power, the turn off of the ICE is overruled. This is done in order to meet the power request to the highest degree possible. The effect of the ICE turn-off level on the fuel consumption has been studied by varying the level from 28% to 33% in steps of 1%. The result is presented in Figure 4.6.

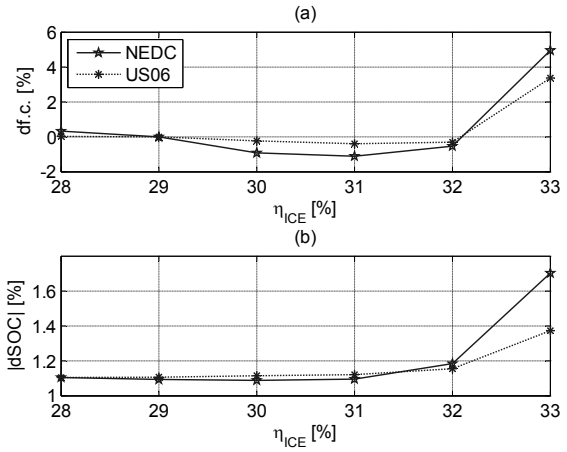

Figure 4.6 Relative change in fuel consumption (a), with regard to the fuel consumption obtained with η_{ICEoff} equal to 29%. Mean SOC deviation (b) with respect to the reference value of 70%.

It can be seen that varying the ICE turn-off level between 28% and 32% only slightly affects the fuel consumption. However, for a level of 33% the fuel consumption increases with about 4% and 6% for the US06 and the NEDC driving cycles, respectively. The reason for this is that the turn-off level is

approaching the maximum efficiency of the ICE. Hence, the ICE is only operated for a very limited number of torque and speed combinations. This result in frequent turn-on and turn-off of the ICE, which results in a low mean ICE efficiency. This can be seen in Figure 4.7.

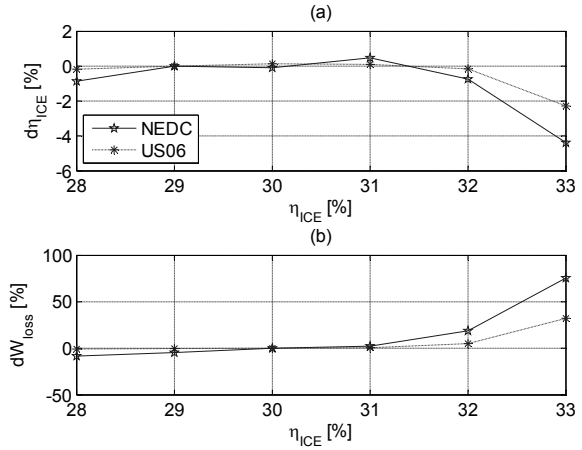

Figure 4.7 Relative change in ICE mean efficiency (a) and total energy loss in the electrical path (b), with regard to the mean efficiency and total loss obtained with η_{ICEoff} equal to 29%.

The figure also shows that, not very surprisingly, as the utilization of the ICE is decreased, the electrical losses increase. The combination of poor ICE mean efficiency and high electrical losses results in lower fuel economy.

ICE Low Pass Filter Time Constant

To prevent the ICE from responding to rapid transients, which leads to higher emission levels, the ICE power request is low pass filtered. As the time constant is made smaller, the difference between the power produced by the ICE and the requested power becomes smaller. Hence, the electrical power that the electrical machines has to supply becomes smaller and smaller. As the time constant approaches zero, the hybrid drivetrain changes from a full hybrid to a power assist hybrid. A power assist hybrid, as the name implies only supports the ICE during heavy accelerations. The drawback with lowering the time constant is that the rapid transients results in increased emission levels [18]. A higher time constant results in a redistribution of the

instantaneous power from the thermal side, i.e. the ICE, to the electrical side, i.e. the electrical machines. Figure 4.8 shows the relative change in fuel consumption and the change in SOC as the ICE filter time constant is changed. The investigated time constants, ranges from 0.2 s to 2s.

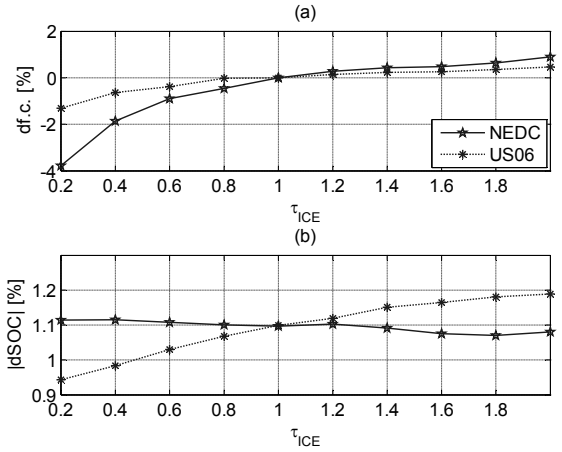

Figure 4.8 Relative change in fuel consumption (a), with regard to the fuel consumption obtained with τ_{ICE} equal to 1s. SOC deviation (b) with respect to the reference value of 70%.

It can be seen that the fuel consumption increases as the filter time constant increases. The reason for this can be traced back to what was stated earlier, i.e. that there will be a redistribution of the power from the ICE to the electrical machines as the time constant is increased. As a consequence of this, the losses in the electrical path will increase. This can be seen in Figure 4.9, which shows the relative changes in the mean ICE efficiency and the total loss in the electrical path.

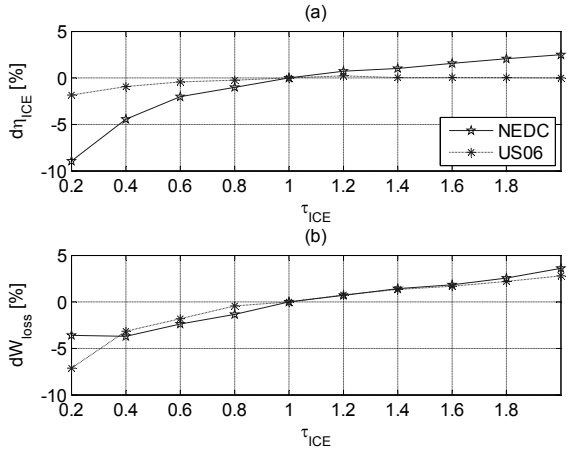

Figure 4.9 Relative change in ICE mean efficiency (a) and the total energy loss in the electrical path (b), with regard to the mean efficiency and total loss obtained with τ_{ICE} equal to 1s.

The figure shows that in spite of the ICE mean efficiency being lower for smaller time constants, the fuel consumption is lower. This is, as was mentioned before, a consequence of the electrical losses being lower.

The gain in fuel consumption when using a low time constant, has to be related to the increased emission levels, originating from the increased bandwidth of the ICE. Hence, the choice of time constant is a trade-off between a relatively modest gain in fuel consumption and higher emission levels. To be able to make the best choice, the actual emission levels has to be considered. It will be assumed that the relatively modest gain in fuel economy is not justifiable to the increased emission levels. Thus, a time constant of 1 s will be used through out the thesis.

Optimal Parameters

In the preceding sections, the influence that each individual control parameter has on the fuel consumption has been discussed. However, it is not a matter of course that the best fuel consumption is obtained by choosing the best parameter according to the individual investigations performed in the preceding sections. It might even be, that such a choice of parameters might result in a controller that does not work properly. Thus, in order to choose

the best combination of control parameters, they have to be investigated together. Figure 4.10 shows the result of several simulations, where the SOC controller gain and the ICE efficiency turn-off level have been investigated together. The ICE low pass filter time constant was here set to 1 s, according to the previous discussion.

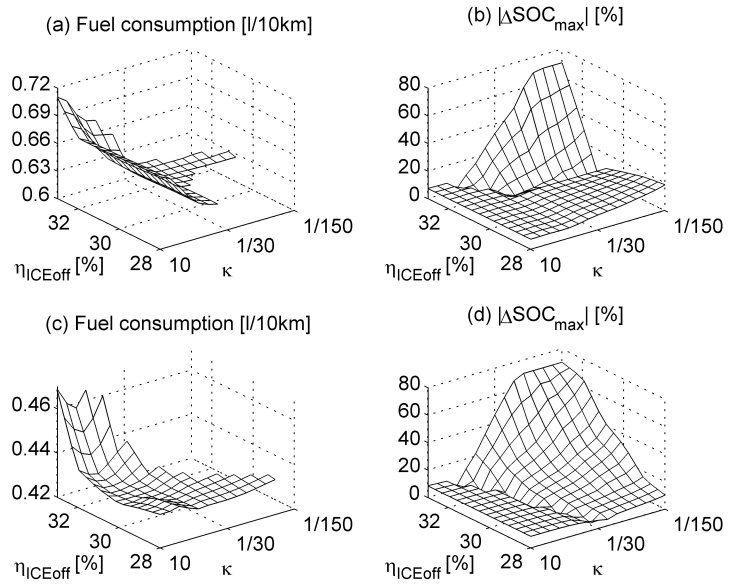

Figure 4.10 Fuel consumption and absolute value of the maximum SOC deviation for the US06 (a, b) and the NEDC (c, d) cycle.

Figure 4.10 shows the fuel consumption and the absolute value of the maximum SOC deviation during each driving cycle. Figure 4.10(a)-(b) and Figure 4.10(c)-(d) shows the results for the US06 and the NEDC cycle, respectively. Combinations of control parameters where the SOC deviation is higher than 15 %, is considered none admissible combinations. The fuel consumption for these combinations is for that reason not presented in the figure. Figure 4.10(a) and (c) both shows that low scaling factors and high η_{ICEoff} results in none acceptable SOC deviations, i.e. over 15 %. This is a consequence of the ICE being in the off-state for a considerable part of the driving cycle and the decreased effort in controlling the SOC. When the ICE

is shut off, the electrical machines step in, resulting in a lower SOC. In addition to this, with the ICE on, the lower SOC controller gain leads to a slow correction of the SOC back to its reference value. The result of this is a dramatic decrease in SOC. Hence, these combinations of control parameters are of now interest. For low scaling factors and low ICE efficiency turn-off levels the SOC deviations are also too high. This phenomenon can only be seen for US06. During heavy decelerations, the SOC increases significantly to recover as much energy as possible. If two decelerations occur close in time, a low SOC controller gain will result in a trend of an increasing SOC, since the correction is not fast enough. These combinations of control parameters will, accordingly not be an admissible choice.

Figure 4.11 shows which combinations of the control parameters that are admissible for NEDC, US06, both of the cycles and those, which are not. It also shows how the control parameters should be selected to achieve minimal fuel consumption. This is symbolized by the black area, and within this area the fuel consumption is 1.5 % within the minimum value.

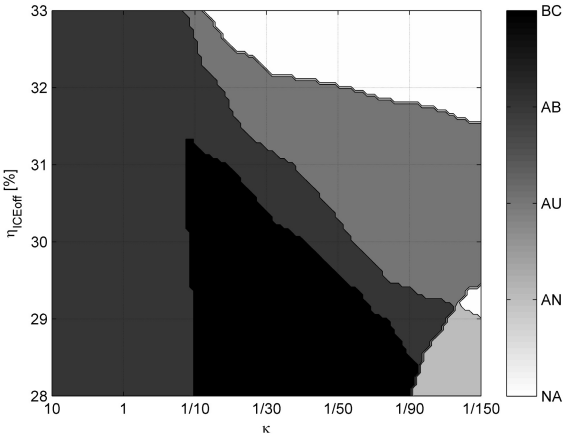

Figure 4.11 Illustrates the admissible and none admissible combinations of the control parameters for the NEDC and the US06 cycle. The abbreviations have the following meaning: Not Admissible, Admissible for NEDC, Admissible for US06, Admissible for Both and Best Choice.

Figure 4.13 shows why the best choice of control parameters falls within the black area shown in Figure 4.11.

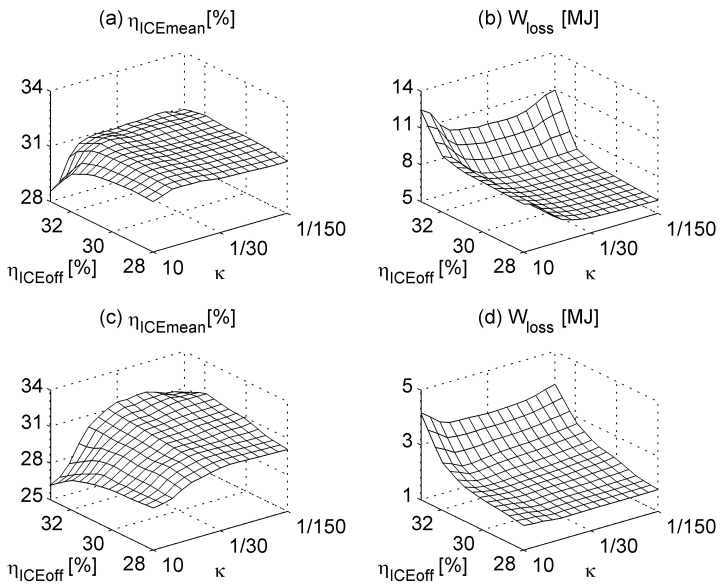

Figure 4.12 ICE mean efficiency and total energy loss in the electrical path for US06 (a, b) and NEDC (c, d).

Three main reasons can be distinguished. The first one is that the SOC deviations are kept within the limit of 15%, the second one is that a high mean efficiency of the ICE is obtained and the last one is that the losses in the electrical path are kept at a reasonable level. All of this together, gives an admissible choice of control parameters that gives a high fuel economy.

Non-Linear Feedback Term

The previous section showed that the SOC controller gain should be chosen rather small, this is, however, in contradiction with keeping the SOC within reasonable limits. This can be solved by replacing the simple SOC controller with a non-linear controller, as proposed in [19] and [20]. The constant SOC controller gain, k_{SOC}, is in the non-linear controller, not kept constant. It will in fact be changed according to a tangent function. Figure 4.13 shows the principle shape of the non-linear gain.

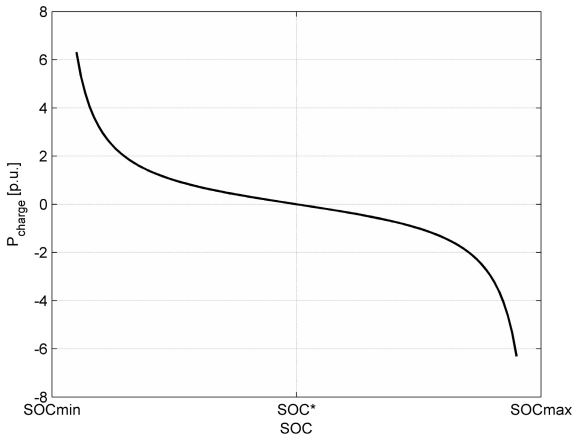

Figure 4.13 Principle shape of the non-linear feedback term.

This will solve the contradiction of having a low gain and avoiding drifts in the SOC. As long as the SOC is within certain limits, the gain will be low. Passing these limits will result in a much higher gain, forcing the SOC back within the limits. The following mathematical description of the non-linear feedback term is presented in [24]

$$P_{charge} = -k \tan\left(\frac{\pi\left(SOC(t) - \left(\frac{SOC_{\max} + SOC_{\min}}{2} \right) \right)}{SOC_{\max} - SOC_{\min}} \right) \qquad (4.14)$$

where P_{charge} is the power delivered to the battery, SOC_{max} and SOC_{min} are the maximum and minimum admissible SOC levels, respectively. The parameter k will here be chosen according to Equation (4.9). This will result in a non-linear feedback term with a lower gain than k_{SOC}, when the SOC is within the limits, and a high gain when the SOC deviation is high. Including the maximum SOC deviation in the relation, Equation (4.14) is changed to

$$P_{charge} = k_{SOC} \tan\left(\frac{\pi}{2}\frac{\left(SOC^{*} - SOC(t)\right)}{\Delta SOC_{\max}}\right) \tag{4.15}$$

where ΔSOC_{max} is the maximum allowed SOC deviation. Note that minus sign has been moved into the tangent function, to be consistent with the linear SOC controller. The variation of the gain for the non-linear feedback term can be obtained, by studying the derivative of Equation (4.15) with respect to the deviation in SOC.

$$\frac{dP_{charge}}{d\Delta SOC} = \frac{-\pi k_{SOC}}{2\Delta SOC_{\max}\cos^{2}\left(\frac{\pi}{2}\frac{\left(SOC^{*} - SOC(t)\right)}{\Delta SOC_{\max}}\right)} \tag{4.16}$$

Figure 4.14(a)-(b) shows the derivative of the non-linear feedback term, i.e. the gain, and the ratio between the gain for the original SOC-controller and the non-linear one. The gains have been normalized with respect to the linear SOC-controller gain and ΔSOC_{max} was chosen to 15%.

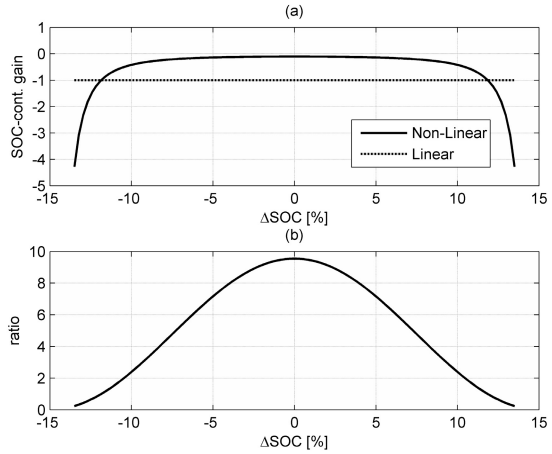

Figure 4.14 SOC-controller gain (a) with linear and non-linear feedback term. Ratio between the linear and non-linear gain.

Figure 4.14 clearly shows the benefits of using the non-linear feedback term. The gain is low in between the predetermined SOC limits and then drastically increases. This is most evident in Figure 4.14 (b) where the ratio between the linear feedback term and the non-linear feedback term is presented. It can be seen that the non-linear feedback gain is approximately 10 times lower for low SOC deviations, whereas it increases rapidly in the vicinity of the SOC limitations. The non-linear gain is actually lower than the linear in 80% of the admissible interval.

The same simulations, which were carried out for determining the optimal controller parameters, were also carried using the non-linear feedback term. The maximum SOC deviation, ΔSOC_{max}, was given the value 10%, in order to assure that the deviation never exceeds 15%. The result of these simulations is presented in Figure 4.15.

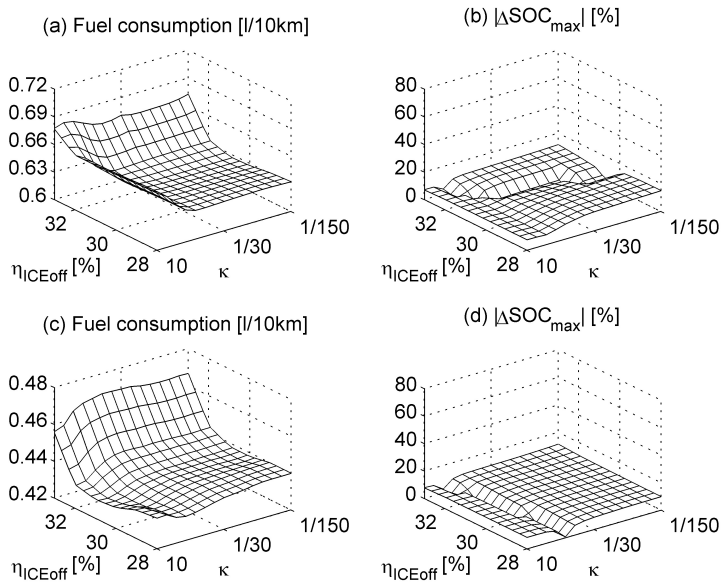

Figure 4.15 Fuel consumption and absolute value of the maximum SOC deviation for US06 (a, b) and NEDC (c, d) using a non-linear feedback term in the SOC-controller.

The simulations show that the maximum SOC deviation is significantly lower with the non-linear feedback term. There are almost no changes in the fuel consumption compared with using a linear feedback term, except for the high scaling factors. The reason for this is what was stated before, that the SOC-controller gain is up to a factor ten smaller, within the predefined limits. Figure 4.16 shows which controller combinations that should be chosen with the non-linear feedback term. It also shows the optimal controller combinations that were obtained with the linear SOC controller.

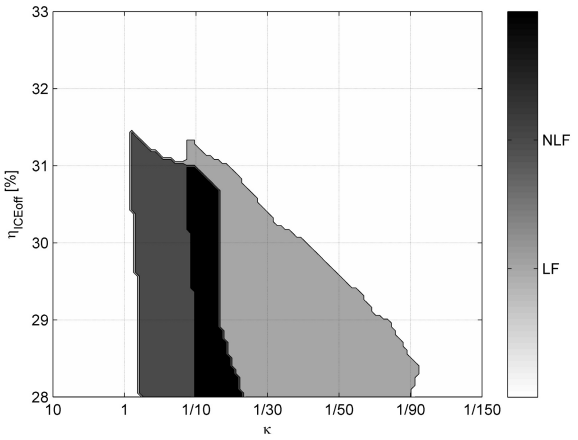

Figure 4.16 Optimal combinations of controller parameters for linear feedback term and nonlinear feedback term. The abbreviations have the following meaning: Linear Feedback, Non Linear Feedback.

As can be seen Figure 4.16, there has been a shift of the area where the controller parameters should be chosen. This is due to the lower gain in the case with the non-linear feedback term.

The difference in minimal fuel consumption, with the two different SOC controllers, is negligible. However, the choice will fall on the non-linear controller, due to its ability to limit the SOC deviation. This is important in order to guarantee a long lifetime of the battery. Chapter 5.4 is dedicated to the comparison of the heuristic control strategy presented here and the results of global optimization.

Robustness

The results in the previous section showed that the optimal operating line strategy does not exhibit any significant cycle-beating trait. This is evident since it was shown that there is a whole range of controller parameters that can be chosen, which will give a satisfactory result, even though the driving cycles are completely different. This robustness can be shown by noticing that the strategy works very well for many different driving cycles. Table 4.4 shows the fuel consumption for four additional driving cycles, with the controller parameters optimized for the US06 and the NEDC according to the previous section.

Table 4.4 Fuel consumption obtained with a conventional vehicle and the reference vehicle, over the FTP72, NYC, HWFET and FIGE cycle. The final SOC for the different driving cycles is also shown.

		FTP72 [1]**[l/10km]** [2][%]	**NYC** [1]**[l/10km]** [2]**[%]**	**HWFET** [1]**[l/10km]** [2]**[%]**	**FIGE** [1]**[l/10km]** [2]**[%]**	**Improve-ment [%]**
Conven-tional	f.c.	0.639[1]	0.954[1]	0.501[1]	0.531[1]	0/0/0
Optimal operating line strategy	f.c.	0.395[1]	0.345[1]	0.429[1]	0.433[1]	-38/-62/ -14/-18
	ΔSOC	77.8[2]	74.7[2]	70.6[2]	73.2[2]	

The FTP72 cycle and the NYC cycle are two urban driving cycles, whereas the HWFET driving cycle is a highway driving cycle. The FIGE cycle contains different driving conditions, such as urban, rural and motorway characteristics. Table 4.4 shows that the gain in fuel consumption varies for the four driving cycles.. The gain in fuel consumption ranges from 14% for the HWFET cycle to 62% for the NYC cycle. In order to show the charge-sustaining characteristics of the strategy, the final SOC is included in the table. It can be seen that the drift in the final SOC is within reasonable levels.

Chapter 5

Dynamic Programming

Dynamic programming (DP) is an useful and important optimization tool, that can be applied to various disciplines. It is used in as different areas as economics, game theory, artificial intelligence, control systems to mention a few. In, for example, control system design, dynamic programming serves as a tool for providing ideal trajectories or paths [21]. DP problems involve making a sequence of decisions in order to optimize some criterion. However, it should be pointed out, that DP is not a specific algorithm that can solve all dynamic programming problems. It should rather be considered as a way of decomposing certain problems into more amenable ones. The theory of DP will here be used to solve the finite horizon optimization problem of determining an optimal control strategy for the reference vehicle, over an in advanced known driving cycle.

5.1 Dynamic Programming Basics

DP is based on Bellman's principle of optimality [22]. The principle states that, the characteristics of a optimal path is, regardless of the initial state and initial control actions, that the subsequent control actions has to be optimal for the remaining problem, with regard to the state resulting from the first decision. The core essence is that all parts of an optimal path are optimal paths themselves [23]. The advantages of DP are that the fundamentals are easy to understand, no advanced mathematics are needed and a true optimum are always guaranteed. However, it has its drawbacks, such as high computational load and the need for high memory storage capacity.

Mathematical Problem Formulation and Implementation

The DP technique can be used to compute the optimal control actions, i.e. the optimal power split and gearshift, over a known driving cycle, to minimize the fuel consumption. The approach used here is to start at the end of the driving cycle and work backwards, which is known as backward DP,

computing the optimal control actions at every time instant. A model of the reference vehicle, discretized for numerical optimization, can be expressed as

$$x(k+1) = f(x(k), u(k), k) \tag{5.1}$$

where *x(k)* is the system state vector, which, in this case, consists of the SOC and the gear position. *u(k)* is the vector of control variables, such as gear shift command, the output torque of the ICE and the output torques of the electrical machines. *k* is the present stage, which represents a time instant of the driving cycle. Each stage of the driving cycle has an associated vehicle speed and torque demand. A general DP problem can be stated as follows [23]

Minimize the cost function

$$J = \sum_{k=0}^{N} L(x(k), u(k), k) \tag{5.2}$$

where

$$x(k+1) = f(x(k), u(k), k) \tag{5.3}$$

and subject to

$$x \in X(k) \subset \Re^n, \quad u \in U(k) \subset \Re^m \tag{5.4}$$

---

where *N* is the length of the driving cycle, *L* is the cost of one single stage and *J*, known as the objective function, represents the total cost. The constraints on the system states, *X(k)*, and the control actions, *U(k)*, can, be summarized as follows

$$
\begin{aligned}
X(k):&\quad \begin{cases} SOC_{\min} \le SOC(k) \le SOC_{\max} \\ g_{\min} \le g(k) \le g_{\max} \end{cases} \\
U(k):&\quad \begin{cases} 0 \le T_{ICE}(k) \le T_{ICE_{\max}}(\omega_{ICE}(k)) \\ T_{FAS_{\min}}(\omega_{FAS}(k)) \le T_{FAS}(k) \le T_{IFAS_{\max}}(\omega_{FAS}(k)) \\ T_{RDU_{\min}}(\omega_{RDU}(k)) \le T_{RDU}(k) \le T_{RDU_{\max}}(\omega_{RDU}(k)) \\ s(k) \in \{-1,0,1\} \end{cases}
\end{aligned}
\tag{5.5}
$$

SOC_{min} and SOC_{max} are the minimum and maximum allowed levels of the SOC, respectively. g_{min} and g_{max} are the lowest and the highest gear number. Apart from the constraints in Equation (5.5), the following constraints has to be included in the optimization

$$
\begin{aligned}
\omega_{ICE_{\min}} &\le \omega_{ICE}(k) \le \omega_{ICE_{\max}} \\
\omega_{FAS_{\min}} &\le \omega_{FAS}(k) \le \omega_{FAS_{\max}} \\
\omega_{RDU_{\min}} &\le \omega_{RDU}(k) \le \omega_{RDU_{\max}} \\
P_{bat\,\min} &\le P_{bat}(k) \le P_{bat_{\max}}
\end{aligned}
\tag{5.6}
$$

The constraints in Equation (5.5) and (5.6) ensures proper operation of the ICE and the electrical machines and prevents the battery from being depleted or overcharged. Apart from these inequality constraint, one equally constraint on the delivered torque is included in order to assure a perfect following of the driving cycle at every time instant

$$
T_{wh}^{*}(k) = \left(T_{ICE}(k) + T_{IFAS}(k)\right)R_i(k) + T_{RDU}(k)R_{RDU} \tag{5.7}
$$

The general DP problem described in (5.2)-(5.4) above can be solved recursively by the use of Bellman's principle of optimality. Let J_k^* represent the minimum cost going from stage k to stage N, starting in state $x(k)$ [24]

$$
\begin{aligned}
J_k^*(x(k)) &= \min_{u(k),\ldots,u(N)} \left[\sum_{j=k}^{N} L(x(j),u(j),j) \right] = \\
&= \min_{u(k)} \left[L(x(k),u(k),k) + \min_{u(k+1),\ldots,u(N)} \sum_{j=k+1}^{N} L(x(j),u(j),j) \right] = \\
&= \min_{u(k)} \left[L(x(k),u(k),k) + J_{k+1}^*(x(k+1),k+1) \right]
\end{aligned}
\tag{5.8}
$$

where J_N^* is equal to

$$
J_N^*(x(N)) = \min_{u(N)} \left[L(x(N),u(N),N) \right] \tag{5.9}
$$

The objective of the optimization is to minimize the fuel consumption, which implies that the fuel energy should be included in the objective function. In order for the vehicle to be charge-sustaining, i.e. to have the same level of SOC in the beginning and the end of the driving cycle, a constraint on the final SOC has to be included in the objective function. If this constraint is left out, the battery will be depleted since no fuel is used when the vehicle is operated in pure electric mode. Also included in the objective function is a penalty on changing gear. This is done in order to prevent frequent gear shifting, which would have a negative effect on the drivability. The objective function can be expressed as [25]

$$
\begin{aligned}
J &= \sum_{k=0}^{N-1} L(x(k),u(k),k) + M(x(N)) = \\
&= W_{fuel}(k) + \beta \left| g(k+1) - g(k) \right| + \alpha \left(SOC(N) - SOC^* \right)^2
\end{aligned}
\tag{5.10}
$$

where α and β are penalty factors for the final value of the SOC and the gear shifting, respectively.

Numerical Computation and Interpolation

Since the vehicle model is nonlinear, the DP problem cannot be solved analytically. Numerical computations have to be used. Hence, to solve Equation (5.8) numerically, the states and the control inputs have to be

quantified into finite grids. The state space and the control inputs are quantified according to [26]

$$\begin{aligned} x &\in \{\xi_1, \xi_2 +, ..., \xi_{X(k)}\} \\ u &\in \{\gamma_1, \gamma_2 +, ..., \gamma_{U(k)}\} \end{aligned} \tag{5.11}$$

At each stage the cost-to-go function J_k^* is evaluated at all state grid points, i.e. at $\{\xi_1, \xi_2 \ldots, \xi_{X(k)}\}$, for all control inputs $\{\gamma_1, \gamma_2 \ldots, \gamma_{U(k)}\}$. The optimal control input for stage k and state i is denoted $u^*(\xi_i,k)$. If the next state, i.e. $f(\xi_i,\gamma_j,k)$, is not a quantified state, J_{k+1}^* has to be interpolated. This procedure is described graphically in Figure 5.1.

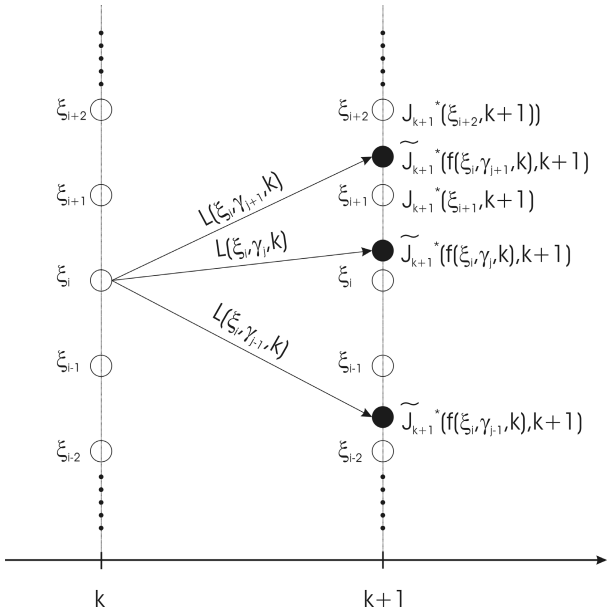

Figure 5.1 Graphical representation of the backward DP algorithm with interpolation of the cost-to-go function [23].

The overall dynamic optimization procedure, including interpolation between states, can summarized in the following steps

$$\begin{aligned}&\text{Step N - 1:}\\&J^*_{N-1}\left(x(N-1),N-1\right)=\min_{u(N-1)}\left[L\left(x(N-1),u(N-1),N-1\right)+M\left(x(N)\right)\right]\\&\text{Step k, for } 0\le k\le N-1\text{, and for } 1\le i\le X(k)\\&J^*_k\left(x(k),k\right)=\min_{u(k)}\left[L\left(\xi_i,u(k),k\right)+\tilde{J}^*_{k+1}\left(f\left(\xi_i,u(k),k\right)\right)\right]\end{aligned} \tag{5.12}$$

where $\tilde{J}^*_{k+1}$ is calculated by interpolating [27] between the two costs belonging to the two states closest to $f(\xi_i,\gamma_j,k)$, see Figure 5.1 above.

5.2 Model Simplification and Implementation

The computation time of for a DP problem is highly dependent on the number of states. In fact, it increases exponentially with the number of states. Hence, there is a trade off between model accuracy and computational burden. A simplified model can be developed by ignoring system dynamics above 1 Hz. This is motivated by the fact that the main objective is to study the fuel consumption during over a driving cycle [25]. Only two states are needed in the simplified model, which are the SOC and the gear number. All of the states are discretized by the use of Euler's method [28]. The vehicle speed is not considered a state since it is given by the driving cycle. The requested torque at every time instant, i.e. stage, can be computed by rearranging Equation (3.1)

$$\begin{aligned}&T^*_{wh}(k)=F^*_{wh}(k)r_w=\\&=m_v r_w\frac{v(k+1)-v(k)}{T_s}+r_w C_r m_v g+\frac{1}{2}r_w\rho_a C_d A_v v(k)^2\end{aligned} \tag{5.13}$$

where Ts is the sampling time, which is set to 1 second, according to the discussion above. Hence, for every stage of the optimization problem, not only the vehicle speed is known, but also the requested torque.

The SOC of the battery can be calculated from Equation (B.1) in Appendix B.

$$SOC(k+1) = SOC(k) + \frac{T_s}{W_{bat}} \frac{P_{EM}(k)}{\eta_{bat}(P_{EM}(k))} \tag{5.14}$$

where P_{EM} is the sum of the electrical machine powers at time instant k and η_{bat}) is the battery efficiency for charging or discharging of that power level. The battery efficiency is modeled as described in Chapter 3.

The 6-speed automatic transmission described in Chapter 3 is modeled as a discrete time system. The state of the system is the gear number, g, and the control input, s, is a signal that can take on the values –1, 0 and 1, which represents a downshift, no shift and an up-shift, respectively. Equation (5.15) describes the modeling of the transmission

$$g(k+1) = g(k) + s(k), \quad \begin{cases} s(k) \in \{0,1\}, & g(k) = 1 \\ s(k) \in \{-1,0,1\}, & 1 < g(k) < 6 \\ s(k) \in \{-1,0\}, & g(k) = 6 \end{cases} \tag{5.15}$$

The ICE and the electrical machines are modeled as described in Chapter 3.

5.3 Simulations and Results

The method of dynamic programming, described in the previous chapter, has been applied to the reference vehicle, in order to investigate the potential of the hybridization. The results from the dynamic programming will serve as a benchmark, and is used to show how close the optimal operating line strategy is to the optimal solution.

Figure 5.2 shows the results from two simulations, where dynamic programming has been used to determine the optimal control actions. The simulation was carried out over the US06 and NEDC driving cycle. The data for the reference vehicle where used, with one distinction, the RDU is not included in the simulation model. This is done in order to clearly show the fundamentals of the hybridization. If the RDU is included, which will be the case later, the regenerated energy will be in the magnitude of the energy used by the electrical machines. The way that the optimal control policy handles recharging of the battery with the ICE, will under these circumstances be lost. Hence, the RDU is, in this first simulation, left out to clearly show all modes of operation.

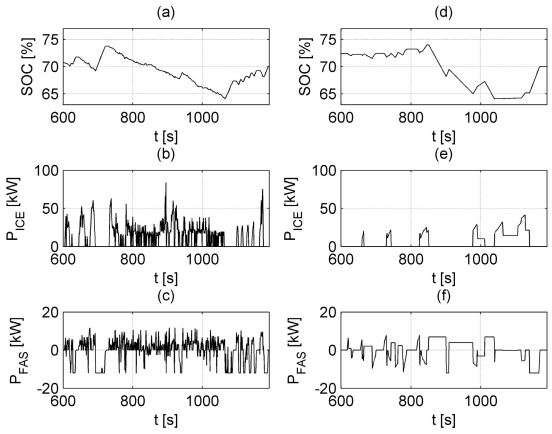

Figure 5.2 Simulation results from the DP for the US06 and the NEDC driving cycle, showing the SOC, the ICE power and the FAS power for both cycles. Only results from the second half of the driving cycles are shown for clarity.

The figure shows that the control strategy is charge-sustaining, i.e. the initial value of the SOC is equal to the end value, which was a constraint used in the objective function. Figure 5.2 shows the ICE and FAS torque for the respective driving cycle. The ICE is used extensively for the demanding US06 driving cycle, whereas for NEDC the ICE is shut off most of time. The ICE is off since low power levels imply poor ICE efficiency. The power flows in the drivetrain can be quantified by using the concept of power split ratio (PSR), that was used in Chapter 4.3. The PSR is here defined as the ratio between the power from the ICE and the requested power from the driver [25], see Equation (5.16)

$$PSR = \frac{P_{ICE}}{P_{wh}^{*}} \tag{5.16}$$

Four different modes of operation can be distinguished; pure electric mode, PSR=0, power assist mode , 0<PSR<1, pure thermal mode, PSR=1, and recharging mode, PSR>1. Note that the PSR is only computed for positive power demands, since it will always be zero during regenerative breaking. Figure 5.3 shows the PSR for the US06 and NEDC driving cycles. The PSR

is in Figure 5.3(a)-(b) and Figure 5.3(c)-(d) shown as a function of the requested torque and the requested power, respectively. The requested torque has been transformed to the output shaft of the ICE, to clearly show the operation of the ICE.

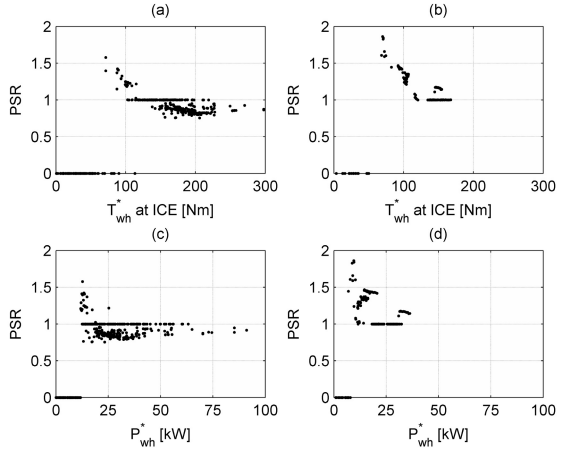

Figure 5.3 PSR for the US06 (a, b) and the NEDC (c, d) driving cycles.

Figure 5.3 clearly shows the four different modes of operation and for which torque levels they are used: the pure electric mode is used for low torque requests, the recharging mode is used for a narrow band of medium torque levels, the pure thermal and the power assist mode is used for medium and high torque levels. The reason for this can be traced back to the fact that low fuel consumption can only be achieved if the ICE is operated with high efficiency. Figure 5.4 shows that high efficiency is accomplished by only operating the ICE above approximately 100 Nm. In addition to this, the ICE speed should be kept quite low, ranging from 1000 rpm up to 4000 rpm. This corresponds to ICE powers ranging from 10 kW to 100 kW. Figure 5.4 shows, apart from the ICE efficiency, the four different modes of operation for the US06 driving cycle.

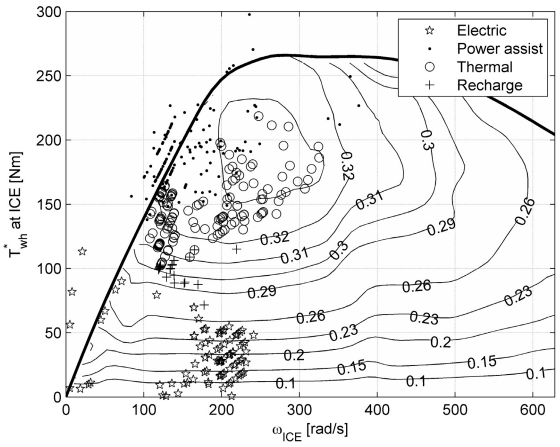

Figure 5.4 ICE efficiency map and the PSR for the four different operating modes.

Figure 5.3(a) and (b) shows that the recharging mode occurs for torque requests ranging from about 70 Nm to 110 Nm. These levels of ICE torques are a good choice for recharging, since the efficiency of the ICE can be increased and at the same time keep the losses in the battery at a reasonable level. For torque references below 70 Nm, the recharging power would have to be very high and the gain in ICE efficiency would be lost due to high battery losses, this implies that the pure electric mode should be used, which also is the case according to Figure 5.3. Pure thermal operation is used in the middle torque region, where the ICE efficiency is high. If the ICE is not able to deliver the requested torque, the electrical machines steps in and assists the ICE. In addition to this, the power assist mode is also used in the middle torque region, i.e. above 150 Nm. The ICE is in fact able to supply the requested torque in these operating points, but that implies that a low gear has to be used. The consequence of a low gear is high ICE speed and low ICE torque, which is in conflict with a high ICE efficiency. The DP power split, consequently suggests a higher gear and operation in the power assist mode, to maintain a high ICE efficiency.

The same simulations have been carried out with the RDU added to the simulation model and the result is presented in Figure 5.5.

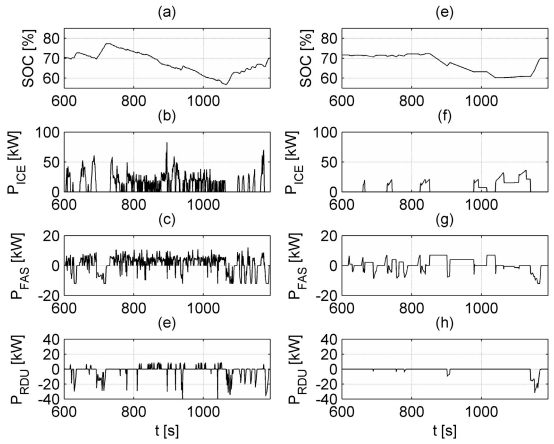

Figure 5.5 Simulation results from the DP for the US06 and the NEDC driving cycle, showing the SOC, the ICE power, the FAS power and the RDU power for both cycles. Only results from the second half of the driving cycles are shown for clarity.

The simulations show that the FAS is used to a greater extent than the RDU. The reason is that the FAS, which is a smaller machine than the RDU, has higher efficiency for low power levels. For the less demanding NEDC the RDU is hardly ever used. However, during deceleration of the vehicle the RDU is used quite extensively to capture as much of the braking energy as possible. The concept of PSR can reformulated, as was done in Chapter 4.3 in order to study the split of the requested electrical machine power between the FAS and the RDU. Figure 5.6 shows the PSR for the electrical machines, where PSR is defined as the ratio between the power from the FAS and the total electrical machine power reference.

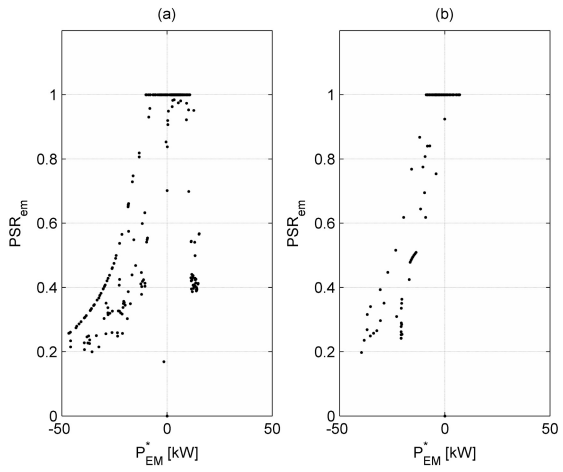

Figure 5.6 PSR for the electrical machines for the US06 (a, b) and the NEDC (c, d) driving cycles.

The results show that for low power references, i.e. below 10 kW, in both motor and generator operation, the FAS is the preferred choice of electrical machine. This is due to the poor efficiency of the RDU for low power levels. For medium positive power references, above 10 kW, the electrical machine torque is split between the two machines and the RDU is assigned approximately 60 % of the power. This increases the total electrical machine efficiency. During deceleration, the total requested electrical power can be rather high. As for the motor operation, the FAS is used for power levels up to 10kW, whereas for higher power levels the RDU has to be used to recover as much energy as possible.

Since two machines are used in this case, more of the braking energy can be captured. In fact, the energy regenerated for the US06 cycle is close to the energy needed for propulsion. Hence, the ICE is never used to recharge the battery. This can be seen in Figure 5.7(a) and (c), where the PSR never exceeds one.

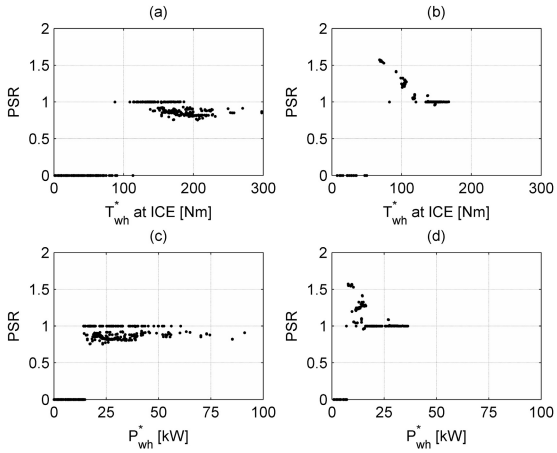

Figure 5.7 PSR for the US06 (a, b) and the NEDC (c, d) driving cycles.

The results from the simulations with the RDU added, is very similar to the results with only one electrical machine. The main difference is, as has been mentioned, that more of the braking energy can be regenerated, which results in a lower fuel consumption. The fuel consumption is decreased from 0.598 l/10km and 0.389 l/10km, when only the FAS is used, to 0.542 l/10km and 0.342 l/10km with the RDU added, for the US06 and NEDC cycle, respectively.

5.4 Dynamic Programming Compared to the Optimal Engine Line Strategy

It has been pointed out that the results from the dynamic programming cannot be implemented as a real-time strategy, since the future driving has to be known in advance. There are, however, suboptimal control strategies based on dynamic programming that uses stochastic models of typical drive behavior [40] or estimation of future driving conditions [13].

The solution to the HEV control problem, i.e. to choose the optimal power split in every time instant, obtained with dynamic programming is here used as a benchmark for the heuristic control strategy. It is hereby possible to quantify the performance of the optimal operating line strategy, by studying the difference in fuel consumption. Table 5.1 presents the fuel consumption

obtained with DP and the optimal operating line strategy, for three different driving cycles. The driving cycles used in the comparison are the NEDC, the US06 and a combined driving cycle, where the first part is the NEDC and the second part is the US06. Included in the table are the fuel consumptions obtained for simulations with a conventional vehicle of the same size and the same engine as the reference vehicle. The vehicle weight is reduced compared to the hybrid counterpart, to compensate for the extra weight of the power electronics and electrical machines.

Table 5.1 Fuel consumption obtained with a conventional and the reference vehicle, over the NEDC, US06 and the combined driving cycle.

	NEDC [l/10km]	**US06 [l/10km]**	**Combined [l/10km]**	**Improvement [%]**
Conventional	0.643	0.762	0.727	0/0/0
Dynamic programming	0.374	0.542	0.490	-41/-29/-33
Optimal operating line strategy	0.400	0.592	0.538	-38/-22/-26
Optimal operating line strategy vs. DP [%]	+7.0	+9.2	+9.8	

Table 5.1 also shows the relative difference in fuel consumption obtained with the optimal operating line strategy and DP. It can be seen that the optimal solution is approximately 9% better for the more demanding driving cycles, the US06 and the combined cycle, and approximately 7% for the less demanding NEDC cycle.

One of the main differences, apart from the preview nature of the DP, is that the optimal operating line strategy is based on optimizing the use of the ICE. The strategy chooses gear to obtain the highest ICE efficiency possible and if the efficiency is lower than a predefined limit, the ICE is turned off. The control strategy obtained with the DP takes the efficiency of all the components into account, and thereby maximizes, not only the ICE

efficiency, but the overall efficiency for the whole HEV. However, since the ICE suffer from much higher losses that the electrical machines, the ICE is the most important to focus on. This can be seen in the relatively small difference in fuel consumption, ranging from 7% to 9%, between the two strategies.

Both of the strategies are, as has been mentioned before, charge-sustaining. There is however a major difference in how the SOC is controlled between the two strategies. The solution to the control problem proposed by the DP is based on the knowledge of the future driving conditions. Hence, this strategy knows when there will be "free" energy, in the form of regenerative breaking, and takes advantage of this by refraining to charge the battery with the ICE. The optimal operating line strategy has, however, no knowledge of the future driving conditions, but relies only on the current system states. This strategy relies on the SOC controller to keep the SOC close to its reference value. The SOC controller is operated at every time instant and tries to force the SOC towards it reference value, this a consequence of not knowing when the mission ends. It should be pointed out, that the will of bringing the SOC back towards its reference value is relieved by lowering the SOC controller gain. As a consequence of the continuously operating SOC controller, the ICE is rarely operated alone. This can be seen in Figure 5.8, where several operating points has a PSR close, but not equal, to one. Hence, there will be a power split between the ICE and the electrical machines, even though a higher overall efficiency might had been obtained by operating the ICE alone.

Figure 5.8 shows that the optimal operating line has, apart from the continuously operated SOC controller, one other drawback. It uses the recharge mode for low power demands. Hence, to achieve high efficiency for the ICE, the ICE power has to be high, resulting in high charging power to the battery. The efficiency of the battery decreases quite significantly with the charging power, and battery losses will increase. It can also be seen that the vehicle is run in all-electric operation for quite high power demands, which also increases the battery losses.

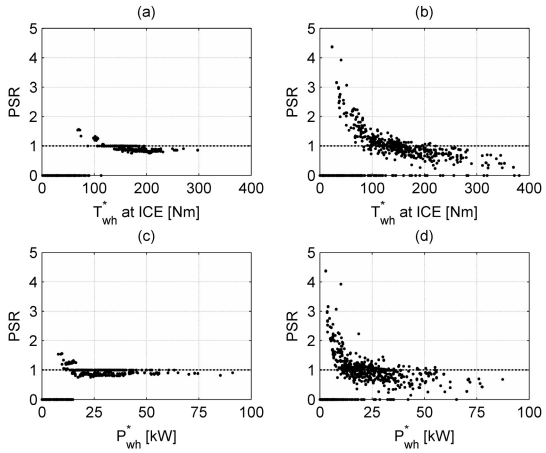

Figure 5.8 PSR obtained with DP, (a) and (c), and the optimal operating line strategy, (b) and (d).

Chapter 6

Conclusions on Energy Management Strategies

The first part of the thesis is devoted to energy management strategies in HEVs and this chapter will present the main results.

The basic function of a heuristic control strategy, named optimal operating line strategy, is discussed. In addition to being simple and robust, the optimal operating line strategy does not exhibit any significant cycle beating trait. It can be used for real-time control, unlike strategies obtained with global optimization, since the strategy only relies upon the current system conditions. The robustness of the strategy is shown by using exactly the same strategy, with the same controller parameters, on four additional driving cycles. The result is satisfactory, with respect to both fuel consumption and the final value of the SOC.

To achieve optimal performance, the control parameters of the heuristic strategies should be tuned. This tuning is often mentioned as a drawback of the rule-based or heuristic control strategies. However, with the optimal operating line strategy, the tuning is relatively simple. Chapter 4.4, discussing the choice of optimal control parameters, showed that the choice is not critical, as long as the following basic rules are followed:

- The ICE turn-off level should not be chosen too close to the maximum efficiency of the ICE, since this gives rise to frequent turn-on and turn-off of the ICE.
- The SOC controller gain should be chosen according to Equation (4.9) in Chapter 4.4, which ensures that the SOC control loop is stable.

- A non-linear feedback term, see Equation (4.15) in Chapter 4.4, should be used. Two benefits are obtained with this choice, the SOC controller gain is lowered within the admissible range of the SOC and large SOC deviations are avoided.
- The ICE filter time constant should be chosen to 1 s, in order to reduce emission levels.

In addition to the choice of controller parameters, one important issue, to assure proper operation of the energy management strategy, is the choice of the number of gears and their individual gear ratio. The importance of this is pointed out, since the core of the strategy is to operate the ICE close to its optimal operating line. It was shown that optimizing the gears, results in a 13% and 6% lower fuel consumption over the combined driving cycle for the 5-speed and 6-speed gearbox, respectively. However, lowering the gear ratios for the 5^{th} and 6^{th} gear for the conventional vehicle, has an negative effect on the acceleration performance. However, for the HEV studied in this thesis, which has two additional torque sources, there was no deterioration of the acceleration performance. In fact, the performance is significantly better for the HEV, where the lower gear ratios are compensated by the additional torque from the electrical machines. It was also shown that the performance goals regarding the acceleration times, 8.0 s for 0-100 km/h and 8.5 s for 80-100 km/h, where met and equal to 7.5 s and 4.6 s for the standard gearbox and 7.8 s and 4.9 s for the optimized gearbox.

Since the vehicle has two electrical machines, there is an additional split to consider, in addition to the split between the thermal and the electrical side. A split based on pre-computed look-up tables, where the split giving the highest electrical machine efficiency, is proposed. It is also pointed out that the split is subordinated the stability control system of the vehicle, and will thereby be overruled for some driving situations.

The task of the energy management strategy is to determine the instantaneous power split between the power sources of the HEV powertrain. The optimal power split, i.e. the solution to the HEV control problem, is computed over a given driving cycle, by the method of DP. The result of this global optimization is then used as a basis for evaluating the real-time heuristic control strategy and serves as a lower bound for the fuel consumption for a given cycle. The results show that the optimal operating line strategy is relatively close to optimal solution. The relative difference in fuel consumption is for the US06 and combined cycle approximately 9% and approximately 7% for the NEDC cycle.

Part II

Control of Electrical Drives in Hybrid Electrical Vehicles

Chapter 7

Rear Drive Unit

On of LU´s tasks in the "MHD-II-project" was to develop a rear drive unit (RDU), based on an electrical machine provided by SAAB. During the project with the RDU it was discovered that the electrical machine had to be rewound for a different voltage level. This was done by the company Tramo in Eslöv. To be able to control the machine a frequency converter was bought from the Finnish company Vacon. The frequency converter was modified to minimize its size.

7.1 Converter

Construction

Vacon has a number of different models of power converters. The converter that turned out be the most suitable choice in the MHD-II-project was the Vacon NXP Liquid-cooled Ch5. The converter was chosen because it fulfilled the desired electrical specifications and its possibilities for size reduction. By reducing the number of DC-capacitors by half, removing the diode rectifier, modify some of the connections and move a capacitor fan, the outer dimensions were significantly reduced. In order to do this some minor mechanical changes had to be carried out.

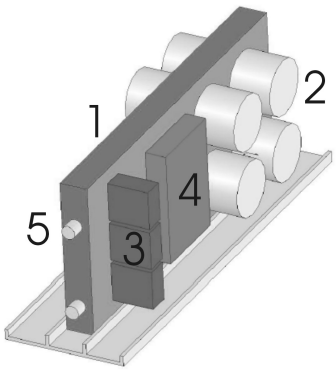

Figure 7.1 The basic structure of the Vacon NXP Liquid-cooled converter.

The basic structure of the converter can be seen in Figure 7.1. The plate in the bottom of the converter (the base plate) is the base on which everything is mounted. The large block perpendicular to the base plate is the heat sink (1) with the connections for the cooling liquid (5) in the short side closest to the observer. The cylindrical parts are the DC-capacitors (2), the rectangular block in the middle of the heat sink is the power semiconductor device (4), the three blocks perpendicular to the heat sink are the current sensors (3). The space on the left side of the heat sink is empty in the version of the converter used in the MHD-II-project. The original converter has its diode rectifier, charge resistor etc mounted there. By removing half of the DC-capacitors from the side of the heat sink opposite of the semiconductor device (the left side in Figure 7.1), the width of the converter was reduced with 35%.

Modification

The modification of the frequency converter was that Vacon delivered the converter with half of the DC-capacitors removed, without one of the cooling fans and with one resistor changed in circuitry for the power supply of the control unit. SAAB Automobile themselves had to cut of the part of the base plate not used. That is the part of the base plate along the left side of the heat sink. SAAB Automobile also removed all plastic details that were not needed. SAAB Automobile built the new chassis.

7.2 Electrical Machine

Basic Machine Parameters

Data for the electrical machine was in the beginning of the project rather limited. For that reason a number of initial measurements with low currents were performed. The machine was connected to a vector control system (dSpace) and ran at no load. The number of poles was determined by counting the number of revolutions in relation to the number of excited phase current periods. The flux linkage of the machine was determined by letting the machine rotate in the test bench and measure the induced voltage. The resistances of the stator windings were determined by applying a DC-voltage between two phases and then measure the current. All of the measured parameters mentioned above are presented in Table 7.1

Table 7.1 Basic machine parameters

Parameter	Symbol	Value
Number of poles	p	8
Flux linkage	ψ_m	0.0697 [Vs]
Stator resistance	R_s	0.068 [Ω]

Rewinding

When a suitable battery had been bought, a decision was made that the machine should be rewound to agree with the voltage of the new battery. The machine was rewound from a DC-voltage of 350 V to 300 V. The number of winding turns was thus decreased with 15% and the diameter of the winding was increased with 7.5%, in order to keep the same copper fill factor. The decrease in the number of winding turns implies lower inductances and this together with the increased winding diameter leads to a lower resistance, but the electrical time constant remains the same. Both quantities are quadratically dependent on the number of winding turns, the inductance according to the definition, the resistance when both the length and the area are linearly dependent on the number of winding turns. The flux from the permanent magnets that is linked with the stator winding, the so-called flux linkage, ψ_m, is also lowered in proportion to the decreased number of winding turns.

7.3 Optimal Current and Field Weakening

To be able to coordinate all of the functions in a vehicle, an overall control system is used. This control system is, in the reference vehicle, named the hybrid controller (HC). One task of the HC is to control the different torque sources, i.e. the ICE, the FAS or the RDU, so that the requsted torque from the driver is accomplished. In the case with the RDU, the HC delivers a reference torque and depending on the torque reference, instantaneous vehicle speed and battery voltage the task of the field weakening controller (FWC) is to produce current references for the current controller (CC). The current references are chosen to give an optimal current, optimal in the sense that the torque-per-current ratio is maximized, under the restriction of keeping the stator voltage and current within their limits [29]. By minimizing the torque-per-current ratio, the copper losses are minimized.

Many field weakening algorithms for IPMSMs have been published. Early works are presented in [30]-[32]. More recent control techniques are described in [33] and [34]. A similar field weakening technology to the one presented in this thesis has been presented in [35]. The suggested control in [35] is also based on pre-calculated look-up tables.

The FWC implemented in the Vacon control unit software is based on comprehensive measurements of the machine. An algorithm is used to process the data from the measurements. The output from the algorithm is look-up tables that are implemented in the inverter control software. The block diagram for the electrical drive of the RDU is shown in Figure 7.2.

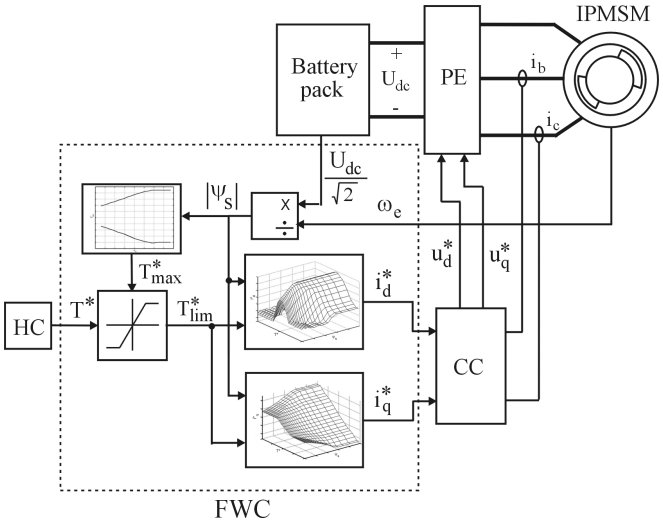

Figure 7.2 Block diagram of the RDU electrical drive.

Even though the FWC is based on measurements, equations describing the ideal characteristics of the machine will be used to explain the function of the FWC.

Optimal Current

The PMSM will in the following sections be studied in a synchronously rotating reference frame, linked to the rotor of the machine. One of the axis of the reference frame, denoted the *d*-axis, is assumed to be aligned with the flux linkage of the rotor [37]. The other axis, referred to as the *q*-axis, is orthogonal to the *d*-axis. It was concluded from the low current measurements that the machine is constructed with buried magnets. Since permanent magnets have almost the same permeability as air, the experienced air gap along the *d*-axis will be wider than along the *q*-axis. The result from this is that the *q*-axis inductance, L_q, will be higher than the *d*-axis inductance, L_d. Apart from the magnetic alignment torque, this saliency ($L_q > L_d$) will give rise to a torque called the reluctance torque [37]. The total mechanical torque of the PMSM, T_m, can be expressed as

$$T_m = \frac{p}{2}\left(\psi_m i_q + (L_d - L_q) i_d i_q\right) \tag{7.1}$$

where ψ_m is the permanent magnet flux linkage and i_d and i_q are the *d*- and *q*-axis stator currents, respectively. The reluctance torque can be used to reduce the stator current for a given torque, i.e. to maximize the torque-per-current ratio. The stator current combinations that maximizes the torque-per-current ratio can be calculated according to the following equations [31]

$$\begin{aligned} |i_s| &= f(T_m^*) \\ i_d^* &= \frac{-\psi_m + \sqrt{\psi_m^2 + 8(L_d - L_q)^2 i_s^2}}{4(L_d - L_q)} \\ i_q^* &= \sqrt{i_s^2 - i_d^2} \end{aligned} \tag{7.2}$$

where i_s is the stator current, T^*_m is the reference torque. A LUT , *f*, is used to map the reference torque into a stator current. The currents i_d^* and i_q^* are the *d*- and *q*-axis current references, respectively. The optimal current trajectory is shown in Figure 7.3, path A.

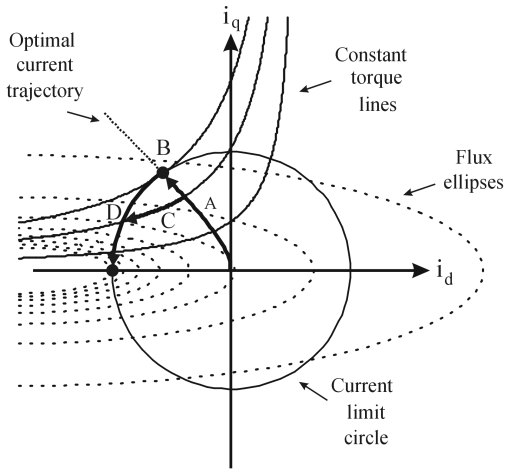

Figure 7.3 Current circle diagram.

The current references can be used as long as the machine is operated below base speed, i.e. in the constant torque region. The currents i_d^* and i_q^* are the references sent to the current controller to obtain the desired reference torque T^*.

As seen in Equation (7.2) the optimal current combination is dependent on the inductances of the machine. In order for the current combination to be optimal it is of importance that the variations of the inductances, due to saturation, is well known. Since the inductance variations are nonlinear, it is difficult to derive an algebraic expression. One way to overcome this problem is to find the optimal current trajectory through careful measurements. The FWC used in the Vacon inverter is based on measurements of the following quantities as functions of the *d*- and *q*-axis currents

$$\begin{aligned} T &= f_T(i_d, i_q) \\ u_d &= f_{u_d}(i_d, i_q) \\ u_q &= f_{u_q}(i_d, i_q) \end{aligned} \tag{7.3}$$

Thus, the torque, T, the direct voltage, u_d, and the quadrature voltage, u_q, have been measured for the combinations of the direct, i_d, and quadrature current, i_q, components spanning the desired operating range of the machine. The measurements have been performed at a fixed electrical frequency, ω_e. Based on these measurements an algorithm has been used to search for the optimal current trajectory. The result has been stored in look-up tables, which are used in the control of the machine. Figure 7.4 shows the measurements carried out on the PMSM used in the RDU.

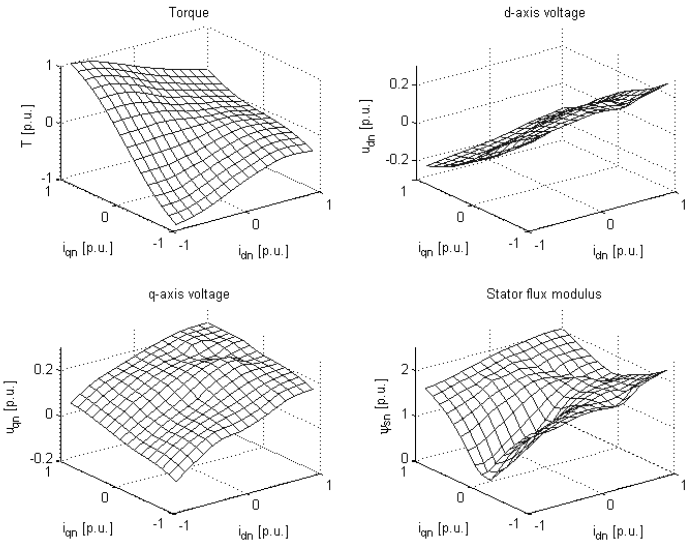

Figure 7.4 Mechanical torque, voltage in the d- and q-direction and stator flux as functions of the currents in the d- and q-direction.

The figure shows how the torque, T, the direct voltage, u_d, the quadrature voltage, u_q, and the stator flux modulus, ψ_s, depends on the stator current components. The stator flux modulus has been derived as follows

$$\begin{aligned} e_d(i_d, i_q) &= u_d(i_d, i_q) - R_s i_d \\ e_q(i_d, i_q) &= u_q(i_d, i_q) - R_s i_q \\ \left|e_s(i_d, i_q)\right| &= \sqrt{e_d(i_d, i_q)^2 + e_q(i_d, i_q)^2} \\ \left|\psi_s(i_d, i_q)\right| &= \frac{\left|e_s(i_d, i_q)\right|}{\omega_e} \end{aligned} \tag{7.4}$$

where e_d and e_q are the induced voltages along the *d*- and *q*-axis and e_s are the total induced stator voltage. The stator flux modulus will be used later in the derivation of the FWC.

Field Weakening

The maximum torque and speed of the PMSM are limited by the maximum output voltage, U_{smax}, and the maximum output current, I_{smax}, of the inverter and the thermal limitations of the machine. The required voltage needed to control the PMSM depends both on the stator current and on the electrical frequency. By assuming steady state and neglecting the influence of the stator resistance the relation between required voltage, current and electrical frequency can be expressed as follows

$$\begin{aligned} u_d &= -\omega_e L_q i_q \\ u_q &= \omega_e \left(\psi_m + L_d i_d \right) \end{aligned} \tag{7.5}$$

The PMSM can be operated with constant torque as long as the required voltage does not exceed the maximum output voltage of the inverter supplying the machine. The maximum output of the inverter is determined by the DC-link voltage, U_{dc}, and the type of PWM-modulation. In order to fully utilize the DC-link voltage, modulation with zero sequence injection is used [37]. This will give a maximum output voltage of the inverter equal to $U_{dc}/\sqrt{2}$.

If no field weakening is used, the consequence of reaching the voltage limit is that the torque will fall to zero. A more severe consequence might be that the current controller becomes unstable. To prevent this and to be able to operate the machine for a wider speed range field weakening must be used. Hence, the required stator voltage should be limited to the maximum output voltage of the converter, yielding the following relation

$$\left(L_q i_q \right)^2 + \left(\psi_m + L_d i_d \right)^2 \le \left(\frac{U_{s\max}}{\omega_e} \right)^2 \tag{7.6}$$

Field weakening with constant torque can be accomplished by forcing the *d*-axis current away from the optimal current trajectory along path C in Figure 7.3. The *d*-axis current can be seen as a demagnetizing current opposing the flux from the permanent magnets keeping the stator voltage within its limit. The current in the field weakening region is not optimal, i.e. maximizes the torque-per-current ratio, but the machine can be operated with constant torque in a wider speed range. By combining Equation (7.1) and (7.6) it can

be seen that the current references depend on the reference torque, the maximum output voltage of the inverter and the electrical frequency. This can be summarized in the following relations

$$\begin{aligned} i_d^* &= f_d(T^*, \omega_e, U_{s\max}) \\ i_q^* &= f_q(T^*, \omega_e, U_{s\max}) \end{aligned} \tag{7.7}$$

The current references will not be calculated using Equation (7.1) and (7.6), but will be based on the measurements mentioned earlier. This will guarantee that the saturation effects of the stator inductances are included in the control. If the relations in Equation (7.7) is used, three dimensional look-up tables have to be implemented in the inverter control software. That can however be avoided by using the relation between stator flux, electrical frequency and maximum output voltage of the inverter. The quantities are related according to

$$|\psi_s| = \frac{U_{s\max}}{\omega_e} \tag{7.8}$$

Hence, the dimension of the look-up tables can be reduced to two if on-line calculation of the stator flux modulus is added in the control software. The current references are then given by

$$\begin{aligned} |\psi_s| &= \frac{U_{dc}}{\sqrt{2}\omega_e} \\ i_d^* &= f_d(T^*, |\psi_s|) \\ i_q^* &= f_q(T^*, |\psi_s|) \end{aligned} \tag{7.9}$$

In order to keep the current within the limits given by the inverter or the thermal characteristics of the machine, the following relation must hold

$$i_d^2 + i_q^2 \le I_{s\max}^2 \tag{7.10}$$

That is, the current must be kept inside the current limit circle shown in Figure 7.3. Once the current limit is reached, the current has to be reduced along path D in Figure 7.3 for increasing speeds and decreasing battery

voltages. The algorithm used to produce the current reference look-up tables takes the current limitation into account.

Algorithm

An algorithm has, as mentioned before, been used to derive look-up tables for the current references. The input to the algorithm is the measurements described above. The basic function of the algorithm is to scan all combinations of possible stator flux levels and reference torques. The algorithm chooses, during the scan, the current combinations according to.

Table 7.2 Selection of current references according to the FWC algorithm.

Current limited	Voltage limited	Action
X	X	Current combinations are chosen along the current limit circle and within the flux ellipses (path D in Figure 7.3).
-	X	Current combinations are chosen along the constant torque lines and within the flux ellipses (path C in Figure 7.3).
X	-	Current combination for maximum torque is used (point B in Figure 7.3).
-	-	Current combinations along the optimal current trajectory are used (path A in Figure 7.3).

Before the algorithm can be used on the measurements, some parameters have to be defined. The minimum stator flux level, ψ_{min}, is determined by the minimum DC-link voltage, U_{dcmin}, and the maximum electrical frequency, ω_{emax}, according to Equation (7.8). The maximum stator flux level, ψ_{max}, should be chosen so that the maximum torque is inside the flux ellipse, see Figure 7.5. This will minimize the dimension of the resulting look-up tables. When these parameters are specified the algorithm scans all combinations of torque reference values, spanning from 0 to T_{max}, and flux levels, spanning from ψ_{min} to ψ_{max}. The result of the algorithm applied on the measurements presented in Figure 7.4 is shown in Figure 7.5.

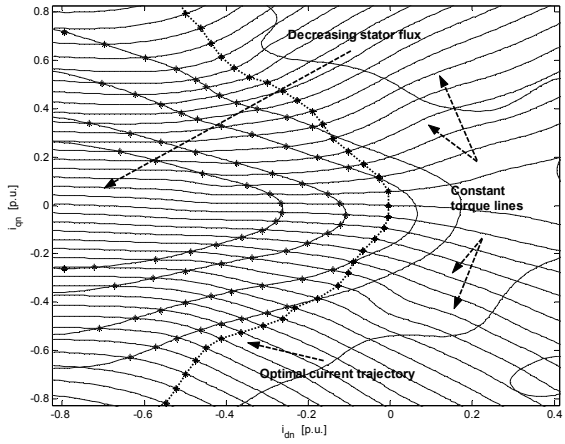

Figure 7.5 Stator current combinations for different torque and flux levels chosen by the algorithm.

It can be seen in Figure 7.5 that the current combinations are chosen according to Table 7.2. The current combinations chosen are stored in two look-up tables, one for the direct and one for the quadrature current reference. Figure 7.6 shows these two look-up tables. For clarity, Figure 7.6 also shows the current references for one fix DC-voltage level as a function of reference torque and electrical frequency.

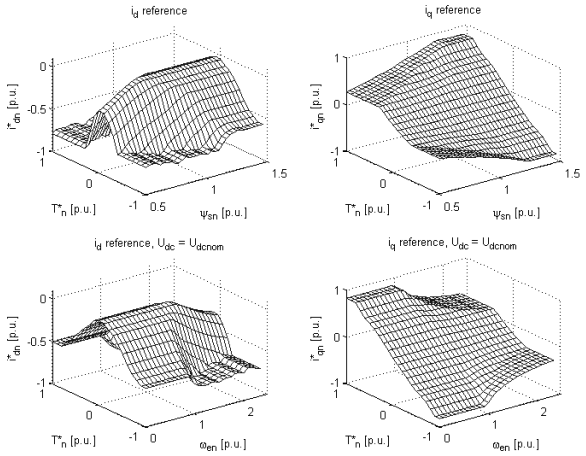

Figure 7.6 Look-up tables for the current references.

The results from the algorithm can be used to calculate the maximum and minimum torques as functions of the stator flux, the result is shown in Figure 7.7.

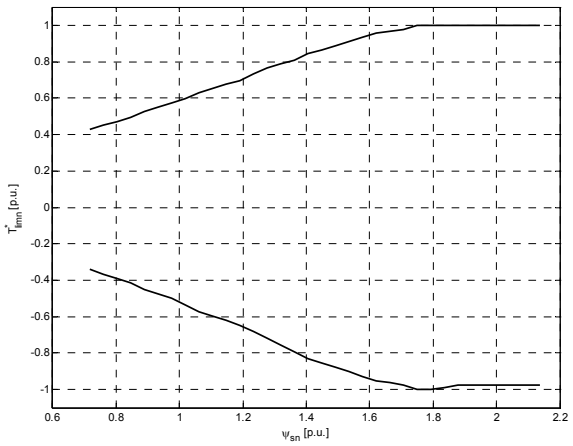

Figure 7.7 Maximum and minimum torque as functions of the stator flux modulus.

The torque limits of the machine are stored in two look-up tables, which are used to limit the torque reference from the HC. This prevents the FWC to read outside the boundaries of the current reference look-up tables, which could lead to instability problems. The use of the torque limit look-up tables are shown in Figure 7.2.

Implementation of Look-up Tables

The two dimensional look-up tables, produced by the algorithm, are implemented as vectors in the controller software. By indexing the vector correct it can be used as a two-dimensional look-up table. Figure 7.8 shows how the two-dimensional look-up table is mapped into a vector.

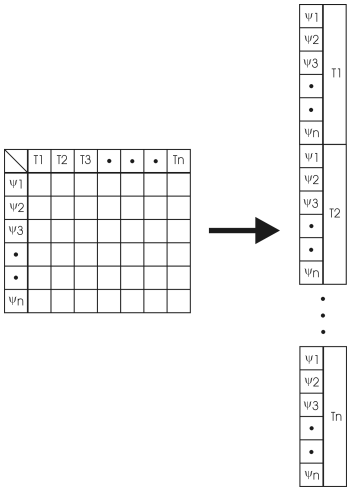

Figure 7.8 Two-dimensional look-up table mapped to a vector.

The correct index for the vector, based on the reference torque and the stator flux, can be calculated as follows

$$
\begin{aligned}
k_T &= \frac{T^*}{\beta_T} \\
k_\psi &= \frac{\psi_s}{\beta_\psi} \\
k_i &= k_\psi + l_\psi k_T
\end{aligned}
\tag{7.11}
$$

where k_T is the torque index, k_ψ is the flux index, k_i is the current index and the constants β_T and β_ψ are the resolutions in the torque and the flux respectively. Furthermore, the constant l_ψ is the number of elements in the flux vector. Because of the limited memory space of the control system a low resolution has been used. In order to still get an accurate control, bilinear interpolation between values has been implemented in the controller software.

Chapter 8

Thermal Modeling and Implementation of Over Temperature Controller

Thermal tests have been carried out in order to determine the thermal characteristics of the machine and to derive a thermal model. It will be shown here that a first order model is enough for describing the winding temperatures, with an acceptable accuracy. The model can be used to calculate the time left before reaching the maximum allowed temperature, which can be useful information for the HC in the task of optimising the energy management. The time calculated is of course highly dependent on the operating point of the machine and the temperature of the cooling liquid. In order to prevent the electrical machine from overheating, some kind of temperature controller has to be implemented. A thermal model will greatly simplify the design of such a controller.

8.1 Measurements

In order to study how different operating points, i.e. different combinations of torque and rotational speeds, affect the temperatures of the windings, seven different measurements have been carried out. The following combinations of torque, T_{mech}, and rotational speed, f_e, have been studied.

Table 8.1 Thermal measurement speed and torque combinations

T_{mech} [Nm]	f_e [Hz]
50	100
0	200
30	200
50	200
0	300
30	300
50	300

During the measurements, the quantities presented in Table 8.2 were recorded.

Table 8.2 List of quantities recorded during the measurements.

Parameter	Description	Unit
T_{w1}	Winding temperature 1	°C
T_{w2}	Winding temperature 2	°C
T_{con}^{in}	Temperature of the cooling liquid entering the converter	°C
T_{con}^{out} $(= T_{RDU}^{in})$	Temperature of the cooling liquid leaving the converter.	°C
T_{RDU}^{out}	Temperature of the cooling liquid leaving the electrical machine.	°C
Q	Water flow rate	L/h
T_a	Ambient temperature	°C
I_{rms}	RMS-value of the phase current	A
I_{dc}	DC-current	A
U_{dc}	DC-voltage	V
P_{con}	Active power leaving the converter	W

Figure 8.1 shows all of the different temperatures presented in Table 8.2 for one specific operating point, T_{mech} = 30 Nm, f_e = 200 Hz.

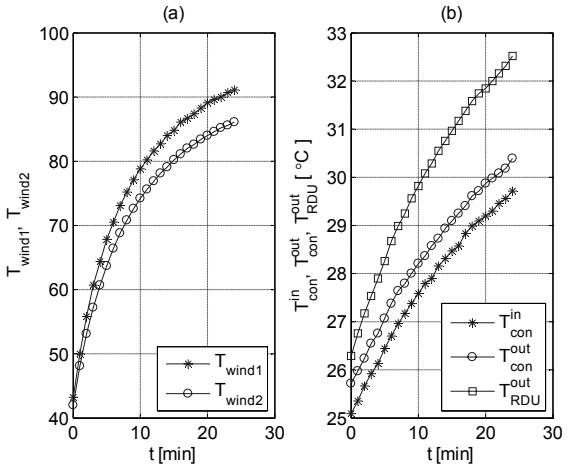

Figure 8.1 Winding temperatures (a) and cooling liquid temperatures (b) for the operating point, T_{mech} = 30 Nm, f_e = 200 Hz

8.2 Modeling and Parameter Estimation

The purpose here for developing a thermal model is to determine how different operating points affect the winding temperature. Since copper losses are the dominating source of power loss, the windings will experience the highest temperature of the consisting parts of the machine [39]. If the winding temperature is kept at a reasonable level there is no risk for overheating the magnets. A thermal model of an electrical machine can be made very complex. The heat transfer in electrical machines is a combination of conduction, convection and radiation. Conduction is transfer of thermal energy, originating from surface contacts of solid materials, whereas convection is heat transfer from surfaces that are in contact with air or cooling fluids [38]. A tempered body will, in addition to this, emit electromagnetic radiation due to its temperature. The machine is modelled as a homogenous body with thermal storage capacity and only thermal energy transfer due to convection is considered. This is a rather rough approximation. However, for the purpose of preventing the windings of the machine from overheating, it will be seen that a first order model is sufficient. The thermal model consists of a power source, representing both the copper and the iron losses in the machine, and a transient thermal impedance. An equivalent circuit of the transient thermal impedance is shown in Figure 8.2.

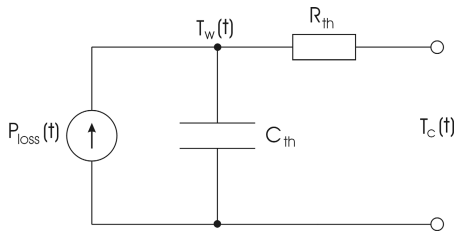

Figure 8.2 Equivalent circuit of the transient thermal impedance.

The parameter P_{loss} represents the losses and R_{th} and C_{th} the thermal resistance and the thermal capacitance, respectively. The thermal resistance is a measure of how a material resists the flow of heat, whereas the thermal capacitance is the ability of a body to store heat as it changes in temperature. Moreover, T_w and T_c are the winding temperature and the cooling liquid temperature, respectively. The differential equation describing the model is given in Equation (8.1).

$$C_{th}\frac{dT_w(t)}{dt} = P_{loss}(t) - \frac{T_w(t) - T_c(t)}{R_{th}} \tag{8.1}$$

This equation can be solved by using the Laplace transform, considering P_{loss} and T_c as input signals.

$$\begin{aligned} &R_{th}C_{th}(s - T_{w0})T_w(s) + T_w(s) = P_{loss}(s)R_{th} + T_c(s) \quad \Rightarrow \\ &\Rightarrow \quad T_w(s) = \frac{P_{loss}(s)R_{th} + T_c(s)}{R_{th}C_{th}s + 1} + \frac{T_{w0}}{R_{th}C_{th}s + 1} \end{aligned} \tag{8.2}$$

The parameter T_{w0} is the initial temperature of the winding. Equation (8.2) can easily be transformed back to the time domain by using partial fraction. The input signal P_{loss} is assumed to change stepwise while the input signal T_c is assumed to be a ramp. Figure 8.1 shows that the later assumption is a good approximation. Hence, T_c will be on the form

$$T_c(t) = k_{T_c}t + T_{c0} \tag{8.3}$$

representing a straight line with the gradient k and the starting temperature T_{c0}. These two parameters are derived based on the measurements for the operating points presented in Table 8.2. Equation (8.2) together with Equation (8.3) can then be transformed to the time domain

$$T_w(t) = \left(\hat{P}_{loss} R_{th} + \hat{T}_{c0} - k_{T_c} R_{th} C_{th}\right)\left(1 - e^{-\frac{t}{R_{th}C_{th}}}\right) + k_{T_c} t + T_{w0} e^{-\frac{t}{R_{th}C_{th}}} \quad (8.4)$$

Equation (8.4) can be simplified to

$$T_w(t) = C\left(1 - e^{-kt}\right) + k_{T_c} t + T_{w0} e^{-kt} \quad (8.5)$$

The parameters k and C are unknown and are estimated from the measurements, by the use of the least-square method. The function in Equation (8.5) is fitted to the temperature measurements for each operating point. There are several different methods for solving nonlinear least squares problems. The method used here is the damped Gauss-Newton method. Since the inverse of the parameter k represents the time constant of the system, it should be independent of the operating point under the assumption that the flow of the cooling liquid is kept constant. Hence, k is kept constant and C, which represents the end temperature of the winding, is determined by least squares. This is done for several different values of the parameter k and the value yielding the smallest residual are chosen. The result of the minimisation is presented in Table 8.3.

Table 8.3 Parameter values obtained from the least square minimization.

k = 0.00264 s^{-1}		Mechanical torque, T_{mech} *[Nm]*		
		0	30	50
Electrical frequency, f_e *[Hz]*	100	X	X	C_{11} = 137
		X	X	C_{12} = 123.5
	200	C_{21} = 45.5	C_{31} = 86.5	C_{41} = 153
		C_{22} = 46	C_{32} = 81	C_{42} = 138.5
	300	C_{51} = 56	C_{61} = 109.5	C_{71} = 170.5
		C_{52} = 56.5	C_{61} = 104.5	C_{72} = 158.5

The optimal k was proven to be 0.00264 s^{-1}, which corresponds to a time constant of 379 s. Figure 8.3 below shows the relative error between the fitted model and the measurements, as a function of time.

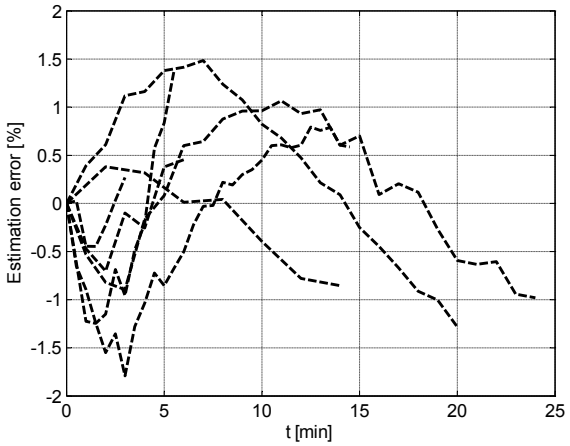

Figure 8.3 Relative error between measurements and fitted curve.

The main thing that can be seen in Figure 8.3 is that a first order model fits the measurements quite well. It should be noted that the maximum error between the measurements and the fitted curve is only 1.8 %, which in this application is considered to be an acceptable error level.

To be able to calculate the end temperature for operating points not measured the model has to be extended to explicitly incorporate both the copper and the core losses. Core losses can be modelled by using Steinmetz equation [39]

$$p_{Fe} = k_h B_p^{\alpha} f + k_e B^2 f^2 \tag{8.6}$$

where p_{Fe} is the specific loss, B_p is the peak value of the flux density, f is the frequency and k_h, and, k_e are machine specific constants, which normally are determined experimentally. The first part of Steinmetz equation is the hysteresis loss and the second part is the eddy current loss. To limit the number of unknowns, Equation (8.6) is simplified to

$$P_{Fe} = K\left|\omega_e \psi_s\right|^{\gamma} \tag{8.7}$$

including a dependency on both the magnetic flux and frequency, where P_{Fe} is the core loss, ψ_s is the stator flux, K and γ are machine specific machine parameters. The final loss model, which incorporates both the copper and the core losses, is equal to

$$P_{loss} = R_s i_s^2 + K\left|\omega_e \psi_s\right|^{\gamma} \tag{8.8}$$

where R_s is the resistance of one stator phase winding, i_s is the stator phase current, and ω_e is the electrical frequency. The final relation for calculating the winding temperature can then be obtained by combining Equation (8.4) and (8.8), yielding

$$T_w(t) = \left(\left(R_s i_s^2 + K\left|\omega_e \psi_s\right|^{\gamma}\right)R_{th} + \hat{T}_{c0} - k_{T_c} R_{th} C_{th}\right)\left(1 - e^{-\frac{t}{R_{th}C_{th}}}\right) + \\ + k_{T_c} t + T_{w0} e^{-\frac{t}{R_{th}C_{th}}} \tag{8.9}$$

By comparing Equation (8.5) and (8.9), the following relation is obtained

$$\left(R_s i_s^2 + K\left|\omega_e \psi_s\right|^{\gamma}\right)R_{th} + \hat{T}_{c0} - k_{T_c} R_{th} C_{th} = C \tag{8.10}$$

There are three unknown parameters that have to be determined and again the methodology of least-squares are used. Equation (8.10) are rearranged to a more suitable form that can be used in the minimization

$$\begin{aligned} & R_s i_s^2 R_{th} + K R_{th}\left|\omega_e \psi_s\right|^{\gamma} R_{th} = C - \hat{T}_{c0} + k_{T_c} R_{th} C_{th} \quad \Rightarrow \\ \Rightarrow \quad & \left\{ \begin{array}{l} a = R_{th} \\ b = K R_{th} \\ c = \gamma \\ X = R_s i_s^2 \\ Y = \left|\omega_e \psi_s\right| \\ Z = C - \hat{T}_{c0} + k_{T_c} R_{th} C_{th} \end{array} \right\} \quad \Rightarrow \quad aX + bY^c = Z \end{aligned} \tag{8.11}$$

The optimal values of the parameters in Equation (8.11) are presented in Table 8.4. These values in combination with the optimal value of the time constant can finally be used to determine the parameters of the transient thermal impedance. The values of these parameters are also presented in Table 8.4.

Table 8.4 Parameter values obtained from the least square minimisation and parameters recalculated to transient thermal impedance parameters.

Parameter	Optimal value	Parameter	Optimal value
a_1	0.161	R_{th1}	0.213
a_2	0.141	R_{th2}	0.183
b_1	1.181	C_{th1}	1782
b_2	1.215	C_{th2}	2066
c_1	0.213	K_1	0.757
c_2	0.183	K_2	0.767
k_1	0.00264	γ_1	1.181
k_2	0.00264	γ_2	1.215

With an estimate of all necessary parameters, a comparison between the final model presented in Equation (8.9), with the optimal parameters presented in Table 8.4, and the measured values are performed and presented in Figure 8.4(b). A comparison between the fitted curve, corresponding to Equation (8.5) and the final model is also carried out and presented in Figure 8.4(a)

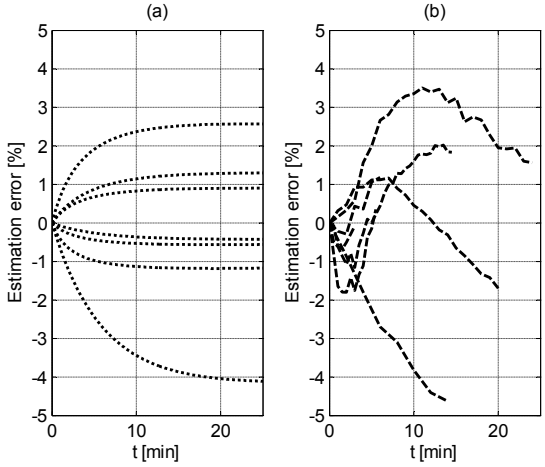

Figure 8.4 Relative error between fitted curve and final thermal model (a) and relative error between measurements and final thermal model (b).

Figure 8.4 shows that the error between the fitted curve and the final thermal model is within 4%. It can also be seen that the maximum error between the final thermal model and the measurements is within 5%.

With the final model determined the end temperature for all different operating points can be calculated. Figure 8.5 shows the end temperature for the combinations of all permitted torques and vehicle speeds. The DC-voltage and the temperature of the cooling liquid are in Figure 8.5 assumed to be equal to 300 V and 25 °C, respectively.

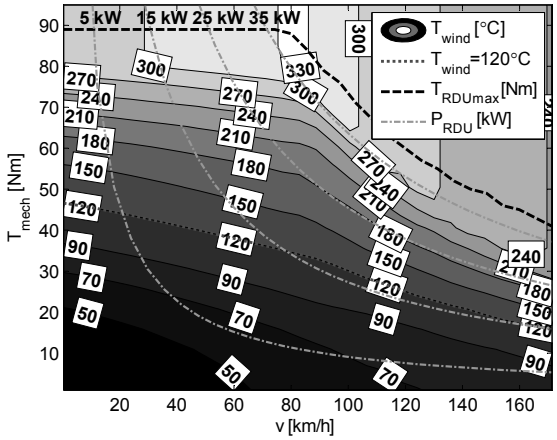

Figure 8.5 Winding end temperature as a function of torque and vehicle speed. Temperature of the cooling liquid and DC-voltage are equal to 25 °C and 300 V, respectively.

Equation (8.9) shows that the end temperature of the windings depends, as expected, both on the torque and vehicle speed. However, Figure 8.5 shows that the end temperature is much more dependent on torque than on vehicle speed. Apart from showing the end temperature for the windings, Figure 8.5 also shows the maximum torque as a function of vehicle speed. The machine enters the field-weakening region when the speed is about 80 km/h. For torque levels above 40 Nm it can be seen that the temperature rises much more quickly in the field weakening region. This is due to the larger current, originating from the demagnetization current, and the fact that the copper losses are the dominating type of losses.

The time constant is, as has been mentioned before, somewhere around 6 minutes. This relatively large lag between power loss and rise in temperature can be utilised to overload the machine, without exceeding the rated temperature. The maximum allowed winding temperature for the IPMSM is 120 °C. If operating points below the maximum temperature curve are chosen the machine can be used in continuous duty. However, only operating the machine in this area would significantly decrease the performances of the traction drive.

In order to make full use of the machine performances, short time use of operating points outside the continuous operating area has to be permitted. This type of operation, when the time of operation is considerably lower than the thermal constant, is often referred to as short time intermittent duty [41]. If this type of operation is permitted, it is possible to overload the machine. Overloading is possible until the temperature reaches its maximum, once this occurs an operating point within the continuous operating area has to be used. The time before reaching the permissible limit can be calculated by rearranging Equation (8.9), yielding

$$t_{120} = -R_{th}C_{th} \cdot \ln \left| \frac{T_{w\max} - \left(\left(R_s i_s^2 + K \left| \omega_e \psi_s \right|^{\gamma} \right) R_{th} + T_c \right)}{T_{w0} - \left(\left(R_s i_s^2 + K \left| \omega_e \psi_s \right|^{\gamma} \right) R_{th} + T_c \right)} \right| \qquad (8.12)$$

Figure 8.6 shows the time it takes for the temperature to reach the permissible limit for all operating points of the machine. This time depends not only on the operation point, but also on the temperature of the cooling liquid, the initial temperature of the machine and the DC-voltage.

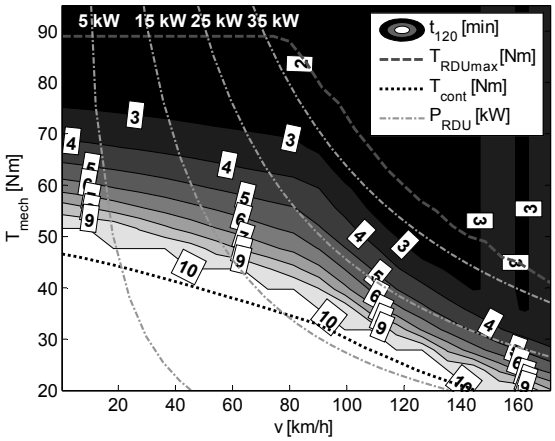

Figure 8.6 Time left, in minutes, before reaching the maximum temperature. The temperature of the cooling liquid is 25 °C, the initial temperature of the winding is 40 °C and the DC-voltage is 300 V.

It can be seen that Figure 8.6 is very similar to Figure 8.5, both of them

having a continuous and an intermittent operating area. Operation points within the intermittent operating area can, in contrast to operation points within the continuous operating area, only be used for a finite time. The shortest operating time, with the initial values stated, is around 2 minutes.

8.3 Thermal Model Validation

In order to determine the accuracy of the proposed thermal model, derived in Chapter 8.2, a test drive with the real hybrid vehicle was carried out. The drive lasted for 5 minutes and contained several accelerations and retardations. The mechanical torque used during the drive and the obtained vehicle speed can be seen in Figure 8.7(a), note that the mentioned quantities are normalized. The temperatures of the stator windings were measured and two of these temperatures are presented in Figure 8.7(b). It can be seen in the figure that the temperatures are fluctuating quite a lot. This is due to the temperatures only having a precision of one degree Celsius. Hence, the measurements where filtered using a moving average filter, taking the mean of 30 adjacent data points.

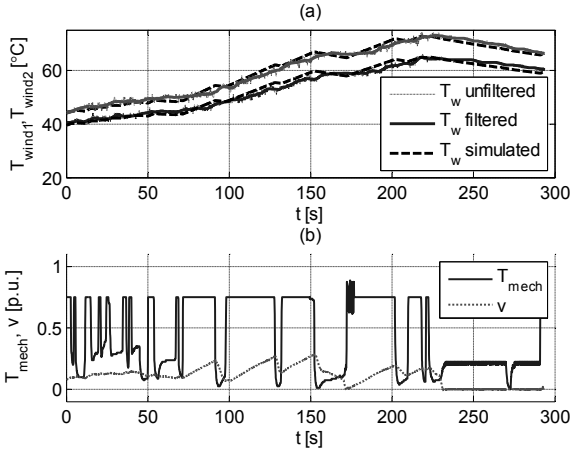

Figure 8.7 Unfiltered, filtered and simulated winding temperatures (a). Normalized torque and vehicle speed logged during the drive.

The logged data from the drive were then used as input to validate the proposed model. A simulink model representing the thermal model where fed with the data obtained from the drive, i.e. reference torque, vehicle speed and

DC-voltage. The simulated winding temperatures are presented in Figure 8.7(a). It should be pointed out that the temperature of the cooling liquid were not available during the drive. However, a reasonable assumption is that the cooling liquid temperature is equal to somewhere near room temperature. Thus the temperature is set to 20°C in the simulation presented in Figure 8.7. To study the effect of a change of the cooling liquid temperature, two simulations with the cooling liquid temperature equal to 15°C and 25°C were carried out. The result of the simulations is shown in Figure 8.8.

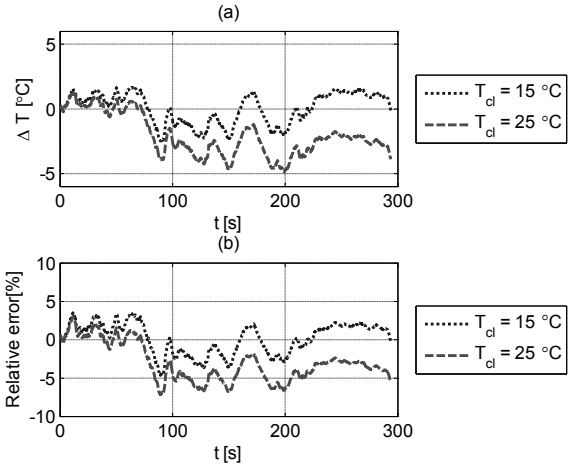

Figure 8.8 Temperature deviation (a) and relative error (b) of the proposed model and measurements for two different cooling liquid temperatures.

It can be seen that, when the cooling liquid temperature is increased from 15°C to 25°C, the maximum temperature deviation increases from 2°C to 5°C and the relative error is increased from 4% to 7%. This shows that the relative error of the proposed model is kept within reasonable limits even though the temperature of the cooling liquid is increased.

To sum up, even though a rather rough thermal model of the electrical machine, the model manages to describe the winding temperature quite accurately. As mentioned above the maximum relative error between measurements and the proposed model is, during the drive, limited to 7%.

8.4 Over Temperature Controller

In order to prevent the machine from overheating, some kind of over temperature controller (OTC) has to be implemented. The basic function of the OTC presented here is to limit the available torque for the HC, when the winding temperature approaches its permissible limit. By limiting the torque, the stator currents will be lower, which corresponds to lower copper losses. The torque available after reaching the limit depends on the DC-voltage, vehicle speed and temperature of the cooling liquid. The structure of the OTC is presented as a block diagram in Figure 8.9.

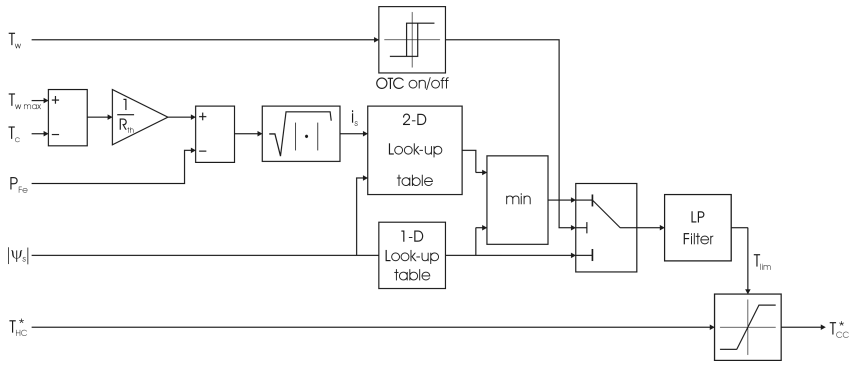

Figure 8.9 Block diagram of the OTC.

The block called *OTC on/off* is a relay, which sets its output high, i.e.OTC on, when the winding temperature reaches 90 % of its permissible limit. If the temperature of the winding starts to decrease the OTC will continue to be on, until the temperature has fallen below 90% of the on-temperature, i.e. below 81% of the permissible limit. If the OTC is off the torque reference from the HC will only be limited by the FWC. However, once the winding temperature reaches its permissible limit, the OTC will be the controller limiting the torque. This is done by using Equation (8.9) and set T_w to the maximum temperature, i.e.120 °C, and solve the equation for the stator current, i_s, see Equation (8.13) below. The stator current are then used together with the stator flux modulus, calculated according to Equation (7.8), to get the corresponding torque from a look-up table. The derivation of the OTC torque limit can be summarised as follows

$$\begin{aligned}
&\left(R_s i_s^2 + K\left|\omega_e \psi_s\right|^\gamma\right)R_{th} + T_c = T_{w\max} \\
&i_s = \sqrt{\frac{T_{w\max} - T_c - R_{th} K\left|\omega_e \psi_s\right|^\gamma}{R_{th} R_s}} \\
&T_{\lim} = f\left(i_s, \psi_s\right)
\end{aligned} \tag{8.13}$$

In order to smoothen the transition between the FWC- and the OTC-limitation of the torque, a low-pass filter has been introduced in the control loop. The cut-off frequency of the filter, ω_c, is chosen to 0.2 rad/s, which corresponds to a rise or fall time, t_r, of approximately 10 s. This choice of cut-off frequency is a reasonable trade-off between the rate of torque capability reduction and overshoot of the winding temperature.

In order to validate the proposed OTC, simulations has been carried out. A model of the RDU and an implementation of the proposed OTC were implemented in Matlab/Simulink. The complete system was simulated using a somewhat modified NEDC driving cycle. The result of the simulation is shown in Figure 8.10 and Figure 8.11. The whole simulation is not shown in the figure for clarity. The initial temperature of the winding is set to 58 °C and the DC-voltage and the temperature of the cooling liquid are assumed constant and equal to 300 V and 25 °C, respectively.

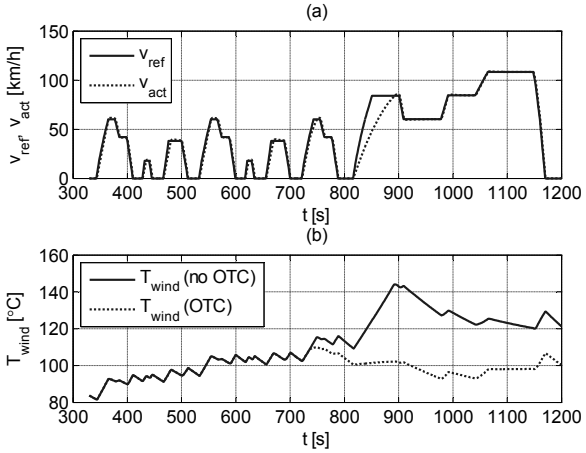

Figure 8.10 Simulation results of the OTC.

Figure 8.10(a) shows the reference speed, v_{ref}, originating from the driving cycle and the actual speed, v_{act}. It can be seen that the actual speed follows the reference speed quiet well. Figure 8.10(b) shows the winding temperature with and without an OTC. In the case with an OTC it can be seen that when the temperature approaches 90% of its permissible limit it is limited, in contrast to the case without an OTC where the temperature continues to increase. The reason for this can be seen Figure 8.11(a).

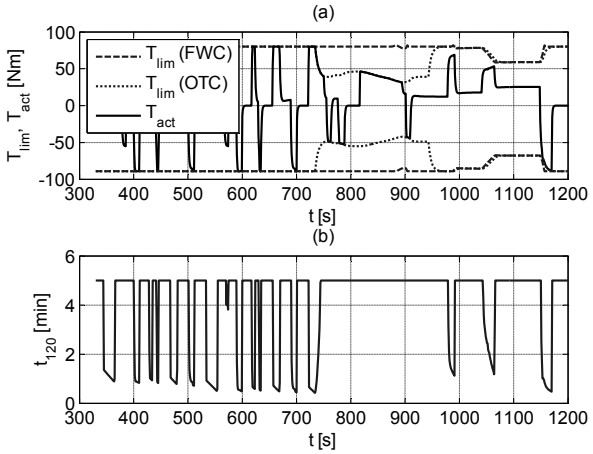

Figure 8.11 Simulation results of the OTC.

Once the temperature hits the limit, the OTC becomes active and the torque is limited according to Equation (8.13). The limitation of the torque is consequently shifted from the FWC to the OTC. When the temperature decreases and the OTC eventually is deactivated, the limitation of the torque is shifted back to FWC. Figure 8.11(b) shows the time, which is denoted t_{120}, that is left before the maximum temperature is reached. It should be noted that for operating points within the continuous operating area, t_{120} will be infinitely large. However, to be able to present t_{120} graphically, all times exceeding 5 minutes has been clamped to this value.

Chapter 9

Conclusions on Control of Electrical Drives in HEVs

The second part of the thesis is devoted to the development of electrically driven rear axle for a HEV. A rear drive unit, consisting of a electrical machine, planetary gear and a differential, was provided by SAAB. Focus is on control and thermal modeling of the electrical machine.

A FWC is developed and implemented in the control system of the converter controlling the electrical machine. The main task of the FWC is to produce current references for the converter current controller given a torque reference, commanded by the superior hybrid controller. The current references are chosen so that the magnitude of the stator flux is kept within its limits, given by the DC-voltage and vehicle speed. The proposed FWC uses pre-calculated look-up tables based on comprehensive measurements of the machine. By using look-up tables, fast dynamic torque control is obtained and machine non-linearities are incorporated in the control. The fast field weakening performance is important in a HEV since the battery voltage undergoes rapid variations, during accelerations. In addition to this, the FWC minimizes the torque-per-current ratio by, for a given torque, using the current combination yielding the minimal stator current. The FWC offers a precise torque control over a wide speed range.

A thermal model for the winding temperatures of the machine is derived. The thermal modeling is carried out in two main steps. In the first step a first order model containing two unknown parameters are used. The unknowns are the end temperature of the winding and the time constant of the system. The parameters are determined by fitting the model to thermal data obtained from several measurements. In step two, a loss model, containing both copper and iron losses, is incorporated in the model. A new model fitting procedure is performed and the final model error is proven to be reasonable small. The

final model has been validated against measurements from a testdrive. The maximum relative difference between the proposed model and the data from the testdrive was only 7%. This level of model accuracy is considered sufficient and no model enhancement is carried out.

Based on the thermal model, an OTC is developed, preventing the machine from overheating. The OTC limits the available torque that can be requested from the HC, when the winding temperature approaches its maximum limit. The torque limitation is made in a smooth manner to maintain drivability. The operation of the OTC is verified by simulations and the results are satisfactory.

Chapter 10

Concluding Remarks and Future Work

10.1 Summary of Findings

The conclusions for the two parts of the thesis have been given in Chapter 6 and Chapter 9 and will here be summarized.

Energy Management in Hybrid Electrical Vehicles

A rather simple heuristic control strategy is discussed. The heuristic control strategy benefits from being simple and robust, and the strategy does not show any significant cycle-beating trait. The strategy can be used in real-time and is not only restricted to simulations. It has also been shown that the often mentioned drawback of heuristic control strategies, i.e. the difficulty in tuning the controller parameters, does not apply to the optimal operating line strategy.

The core of the operating line strategy is to operate the ICE along its optimal operating line, i.e. where the highest efficiency is achieved for every given power level. In order to accomplish this, it is important that the correct number of gears and the correct individual gear ratios are chosen. As a consequence of this, the importance of adapting the gearbox to the hybrid powertrain has been pointed out. Optimization of the gear ratios for a 5- and 6-speed gearbox shows that the fuel consumption is decreased with 13% and 6%, respectively. This is accomplished without any decrease in the acceleration performance compared to the conventional vehicle. Both the standard and the optimized 6-speed gearbox proved to fulfill the acceleration goals stated.

Since the vehicle has two electrical machines, there is an additional split to consider, in addition to the split between the thermal and the electrical side. A split based on pre-computed look-up tables, where the split giving the highest electrical machine efficiency, is proposed. It is also pointed out that the split is subordinated the stability control system of the vehicle, and will there by be overruled for some driving situations.

In order to evaluate the performance of the optimal operating line strategy, in terms of fuel consumption, global optimization is used to obtain an optimal solution to the HEV control problem. The global optimization method used is the DP and the results show that the optimal operating line strategy gives a relatively near-optimal result. The relative difference in fuel consumption is for the US06 and combined cycle approximately 9% and approximately 7% for the NEDC cycle.

Control of Electrical Drives in Hybrid Electrical Vehicles

A FWC which offers fast field weakening performance and which minimizes copper losses is proposed. The FWC is effective and simple since it is based on look-up tables. The look-up tables are obtained from comprehensive measurements of the machine. The use of look-up tables has two advantages, fast dynamic torque control and the incorporation of machine non-linearities in the control. Fast field weakening performance is important, since the battery voltage in HEVs is subject to large variations.

It has been shown that a rather accurate thermal model can be obtained using only a first order model. A simple thermal model, with an incorporated loss model is proven to give a reasonable accuracy for the winding temperature. The model parameters is obtained by fitting the proposed model to data obtained from several measurements. The proposed model is validated against a test drive with the reference vehicle, and the relative error for the winding temperature was limited to 7%.

The proposed thermal model forms the basis for the development of a over temperature controller. The task of the OTC is to limit the available torque that can be requested from the overall hybrid controller, to prevent the machine from overheating. To maintain drivability, the torque limitation is lowered gradually. The OTC has been implemented in the simulation model of the reference vehicle and the results are satisfactory.

10.2 Future Work

This section is devoted to ideas of future work, which would be a complement to the results presented in thesis.

The heuristic control strategy that has been discussed and optimized in the thesis has not been validated experimentally. It would be of great interest to see the actual performance of the strategy implemented in the reference vehicle and compare the result to the simulation results. One other aspect of the implementation in a real vehicle is the study of the drivability. How the driver will experience the ICE being shut off for some driving conditions, is an interesting issue that should be investigated further.

The performance criteria for the control strategy studied in the thesis have been the fuel consumption. Low fuel consumption will give rise to low carbon dioxide emission levels. However, this is not the only emitted emission and nothing has been said about other emissions, such as unburned hydrocarbons (HC), carbon monoxide and oxides of nitrogen (NO_x). Extending the simulation model presented in the thesis with an emission model would be one of the main goals for future work.

Experimental investigations of the proposed over temperature controller would be of interest, since it has only been validated through simulations.

The thermal measurements has shown that the RDU can be run at its present maximum torque level for up to 2 minutes. This indicates that the maximum torque level could be increased, with better acceleration performance as a result.

References

[1] K. T. Chau and Y.S. Wong, "Overview of Power Management in Hybrid Electric Vehicles", *Energy Conversion and Management 43*, Hong-Kong, Hong-Kong, , April 25, 2001, pp. 1953-1968.

[2] Hybrid Synergy Drive Information Terminal presented by Toyota, *www.hybridsynergydrive.com/en/un_definition.html*, 2007-03-15.

[3] "Comparing the Benefits and Impacts of Hybrid Electric Vehicle Options", *EPRI*, Palo Alto,CA: 2001, 1000349.

[4] Y. Gao, M. Ehsani and J. Miller, "Hybrid Electric Vehicle: Overview and State of the art", *IEEE International Symposium on Industrial Electronics*, Vol.1, pp 307-315, 2005.

[5] Ilya Kolmanovsky, Michiel van Nieuwstadt, Jing Sun, "Optimization of Complex Powertrain Systems for Fuel Economy and Emissions", *IEEE International Conference on Control Applications*, Hawaii,USA, Aug. 22-27, 1999, pp. 833-839.

[6] J. Heywood, "Internal Combustion Engine Fundamentals", *McGraw-Hill*, New York, NY, USA, 1989.

[7] M. Alaküla, C. Andersson, K. Jonasson and B. Simonsson, "Hybrid Drive Systems for Vehicles part 1", *Department of Industrial Electrical Engineering and Automation*, Lund University, Lund, 2006.

[8] S.M. Lukic and A. Emado, "Modeling of Electric Machines for Automotive Applications Using Efficiency Maps", *IEEE Electrical Insulation Conference and Electrical Manufacturing & Coil Winding Technology Conference*, 2003, pp. 543-550.

[9] N. Mohan, T. M. Undeland, W.P. Robbins, "Power Electronics: Converters, Applications, and design.", 2nd edition, *John Wiley and sons, Inc.*, New York, USA, 1995.

[10] G. Paganelli, G. Ercole, A. Brahma, Y. Guezennec, G. Rizzoni, "General Supervisory Control Policy for the Energy Optimization of

Charge-Sustaining Hybrid Electric Vehicles", *JSAE Review 22*, 2001, pp. 511-518.

[11] V. H. Johnson, K. B. Wipke, D. J. Rausen, "HEV Control Strategy for Real-time Optimization of Fuel Economy and Emissions", *SAE 2000 World Congress*, SAE 2000-01-1543, Detroit, USA.

[12] M. Salman, N. J. Schouten, N. A. Kheir, "Control Strategies for Parallel Hybrid Vehicles", *Proceedings of the American Control Conference*, Chicago, Illinois, June , 2000, pp. 524-528.

[13] C. Musardo, G. Rizzoni, B. Staccia, "A-ECMS: An Adaptive Algorithm for Hybrid Electric Vehicle Energy Management", *Proceedings of the 44th IEEE Conference on Decision and Control, and the Eupopean Control Conference 2005*, Seville, Spain, Dec. 12-15, 2005, pp. 1816-1823.

[14] C.-C. Lin, J.-M. Kang, J.W. Grizzle, H. Peng, "Energy Management Strategy for a Parallel Hybrid Electric Truck", *Proceedings of the American Control Conference*, Arlington, VA, Hune 25-27, 2001, pp. 2878-2883.

[15] A. Brahma, Y. Guezennec, G. Rizzoni, "Optimal Energy Management in Series Hybrid Electric Vehicles", *Proceedings of the American Control Conference*, June, 2000, pp. 60.64.

[16] S. Delprat, J. Lauber, T. M. Guerra, J. Rimaux, "Control of a Parallel Hybrid Powertrain: Optimal Control", *IEEE Transactions on Vehicular Technology*, Vol. 53, No. 3, May, 2003, pp. 872-881.

[17] L. Guzzella, A. Sciarretta, "Vehicle Propulsion Systems: Introduction to Modeling and Optimization", *Springer-Verlag*, Berlin, Germany, 2005.

[18] K. Jonasson, "Analysing Hybrid Drive System Topologies", Licentiate Thesis, *Department of Industrial Electrical Engineering and Automation*, Lund University, Lund, Sweden, 2002.

[19] P. Rutquist, "On Infinite-Horizon State-Constrained Optimal Control – With Application to a Fuel Cell APU", Licentiate Thesis, *Department of Signals and Systems*, Chalmers University of Technology, Gothenburg, Sweden, July, 2005.

[20] P. Rutquist, C. Breitholz, T. Wik, "An Eigenvalue Approach to Infinite_Horizon Optimal Control", *Proceedings of the 16th IFAC World Congress*, Prague, Czech Republic, 2005.

[21] R. D. Robinett III, D. G. Wilson, G. R. Eisler, J. E. Hurtado, "Applied Dynamic Programming for Optimization of Dynamical Systems", *Society for Industrial and Applied Mathematics*, USA, 2005.

[22] R. Bellman, "Dynamic Programming and Modern Control Theory", *Academic Press*, New York, USA, 1965.

[23] A. P. de Madrid, S. Dormido, F. Morilla, "Reduction of the Dimensionality of Dynamic Programming: A Case Study", *Proceeedings of the American Control Conference*, San Diego, California, USA, June, 1999, pp. 2852-2856.

[24] S. Petterson, B. Egardt, F. Bruzelius, "Powertrain Modelling & Control", *Gröna bilen*, Göteborg 2006.

[25] C.-C. Lin, H. Peng, J.W. Grizzle, J.-M. Grizzle, "Power Management Strategy for a Parallel Hybrid Electric Truck", *IEEE Transactions on Control Systems Technology*, Vol. 11, No. 6, November, 2003, pp. 839-849.

[26] J.-M. Kang, I. Kolmanovsky, J. W. Grizzle, "Approximate Dynamic Programming Solutions for Lean Burn Engine Aftertreatment", *Proceedings of the 38th Conference on Decision & Control*, Phoenix, Arizona, USA, December, 1999, pp. 1703-1708.

[27] J.-M. Kang, I. Kolmanovsky, J. W. Grizzle, "Dynamic Optimization of Lean Burn Aftertreatment", *Journal of Dynamic Systems, Measurement, and Control*, Vol. 123, June 2001, pp. 153-160.

[28] L. Råde, B. Westergren, "Mathematics Handbook for Science and Engineering", *Studentlitteratur*, Lund, Sweden, 1998.

[29] J. Ottosson, M. Alaküla, "A Compact Field Weakening Controller Implementation", *Symposium on Power Elecronics, Electrical Drives, Automation & Motion*, Taormina, Italy, May 2006.

[30] S. Marimoto, Y. Takeda, T. Hirasa, K. Taniguchi, "Expansion of Operating Limits for Permanent Magnet Motor by Current Vector Control Considering Inverter Capacity", *IEEE Transaction on Industry Applications*, Sep/Oct 1990, pp. 866-871.

[31] J.-M. Kim, S.-K. Sul, "Speed Control of Interior Permanent Magnet Synchronous Motor Drive for the Flux Weakening Operation", *IEEE Trans. Industry Applications*, Jan./Feb. 1997, pp. 43-48.

[32] S. Macminn, T. Jahns, "Control Techiques for Improved High-Speed Performance of Interior PM Synchronous Motor Drives", *IEEE Transactions on. Industry Applications*, Sep./Oct. 1991, pp. 997-1004.

[33] N. Bianchi, S. Bolognani, M. Zigliotto, "High-Performance PM Synchronous Motor Drive for an Electrical Scooter", *IEEE Transactions on Industry Applications*, Sep./Oct. 2001, pp. 1348-1354.

[34] W. Soong, N. Ertugrul, "Field-Weakening Performance of Interior Permanent-Magnet Motors", *IEEE Transactions on Industry Applications*, Sep./Oct. 2002, pp. 1251-1258.

[35] B.-H. Bae, N. Patel,S. Schulz, , S.-K. Sul, "New Field Weakening Technique for High Saliency Interior Permanent Magnet Motor", *Industry Applications Conference*, 38th IAS Annual Meeting, 2003, IEEE, pp. 898-905.

[36] L. Harnefors, H.-P. Nee, "Control of Variable Speed Drives", *Electrical Machines and Power Electronics Department of Electrical Engineering Royal Institue of Technology*, Sweden, 2000, pp. 49-53.

[37] M. Alaküla; "Power Electronic Control", *Department of Industrial Electrical Engineering and Automation*, Lund University, Sweden, 2003, pp. 101-103.

[38] Y.-K. R Chin, "A Permanent Magnet Traction Motor for Electric Forklifts – Design and Iron Loss Analysis with Experimental Verifications", Doctoral Thesis, *Royal Institute of Technology*, Stockholm, Sweden, 2006.

[39] F. Sahin, A.J.A. Vandenput, "Thermal Modeling and Testing of a High-Speed Axial-Flux Permanent-Magnet Machine", *The International Journal for Computation and Mathematics in Electrical and Electronic Engineering*, Vol. 22, No. 4, 2003, pp. 982-997.

[40] L. Johanesson, "On Energy Managemnet Strategies for Hybrid Elctric Vehicles", Licentiate Thesis, *Department of Signals and Systems*, Chalmers University of Technology, Gothenburg, Sweden, 2006.

[41] W. Leonhard, "Control of Electrical Drives", 3rd edition, *Springer-Verlag*, Germany, 2001.

[42] A. Sciaretta, M. Back and L. Guzzella, "Optimal Control of Parallel Hybrid Electric Vehicles", *IEEE Transactions on Control Systems Technology*, Vol. 12, No. 3, May 2004,pp. 352-363.

Appendix A

Battery Model

The battery model used in this thesis is based on the simple circuit model shown in Figure A.1. It consists of a voltage source and a series resistance.

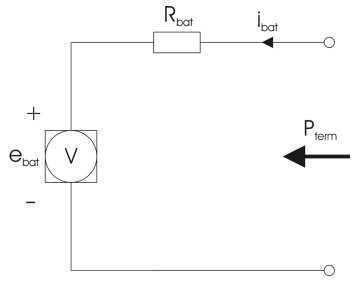

Figure A.1 Battery model.

The voltage of the internal voltage source, e_{bat}, and the internal resistance, r_{bat}, have both a nonlinear dependency on the SOC. Thus, this rather simple model can be made quite accurate since e_{bat} and r_{bat} are based on extensive measurements.

The terminal power, P_{term}, entering the battery can be expressed as

$$P_{term} = e_{bat} i_{bat} + r_{bat} i_{bat}^2 \tag{A.1}$$

where the current i_{bat} can be solved for, yielding the following expression

$$i_{bat} = -\frac{e_{bat}}{2r_{bat}} + \sqrt{\left(\frac{e_{bat}}{2r_{bat}}\right) + \frac{P_{term}}{r_{bat}}} \tag{A.2}$$

The losses in the battery is

$$P_{loss} = r_{bat} i_{bat}^2 \tag{A.3}$$

and the efficiency can finally be derived as

$$\eta_{bat} = \frac{P_{term} - P_{loss}}{P_{term}} \tag{A.4}$$

Hence, the battery efficiency depends both on SOC and on the rate of power either entering or leaving the battery. The SOC variations can be expressed as

$$Q_{\max} \frac{dSOC}{dt} = i_{bat}(t) \tag{A.5}$$

where Q_{max} is the maximum charge of the battery. This expression can be transformed to the following expression

$$W_{bat} \frac{dSOC}{dt} = P_{term}(t) - P_{loss}(t) \tag{A.6}$$

by replacing charge with energy and current with power. W_{bat} is the specific battery energy presented in Table 3.4. Taking the integral of this expression, yields the SOC-variations as a function of time

$$SOC(t) = SOC(t_0) + \frac{1}{W_{bat}} \int_{t_0}^{t} P_{term}(v) - P_{loss}(v)\, dv \tag{A.7}$$

Appendix B

SOC Controller Gain

The derivation of the SOC controller gain k_{SOC} is based on Equation (A.6) and Equation (4.7). The two equations are repeated here for clarity.

$$W_{bat}\, pSOC = P_{term}(t) - P_{loss}(t) = P_{EM}\,\eta_{bat}\,\eta_{EM}^{-sign(P_{EM})} \tag{B.1}$$

$$P_{EM}(t) = \frac{p\tau_{ICE}}{1 + p\tau_{ICE}}\left(P_{wh}^{*}(t) - \frac{k_{SOC}}{p\tau_{ICE}}\left(SOC^{*} - SOC(t)\right)\right) \tag{B.2}$$

By combining and rearranging Equation (B.1) and (B.2), the transfer function for the SOC can be obtained.

$$SOC(t) = \frac{\eta_{bat}\eta_{EM}^{-sign(P_{EM})}}{W_{bat}}\left(\frac{\frac{k_{SOC}}{W_{bat}}}{p^2 + \frac{1}{\tau_{ICE}}p + \frac{\eta_{bat}\eta_{EM}^{-sign(P_{EM})}k_{SOC}}{W_{bat}}}SOC^{*} - \right.$$
$$\left. - \frac{p\tau_{ICE}}{p^2 + \frac{1}{\tau_{ICE}}p + \frac{\eta_{bat}\eta_{EM}^{-sign(P_{EM})}k_{SOC}}{W_{bat}}}P_{wh}^{*}\right) \tag{B.3}$$

P_{wh}^{*} is here considered a disturbance. The poles for the open loop transfer function can be computed by considering the characteristic equation and compare it with a standard characteristic equation for a second order system.

$$\begin{cases} p^2 + 2\varsigma\omega_n p + \omega_n^2 \\ p^2 + \dfrac{1}{\tau_{ICE}} p + \dfrac{\eta_{bat}\eta_{EM}^{-sign(P_{EM})} k_{SOC}}{W_{bat}} \end{cases} \Rightarrow \begin{cases} \dfrac{1}{\tau_{ICE}} = 2\varsigma\omega_n \\ \dfrac{\eta_{bat}\eta_{EM}^{-sign(P_{EM})} k_{SOC}}{W_{bat}} = \omega_n^2 \end{cases} \tag{B.4}$$

ζ is the relative damping of the system and has to be chosen. The relative damping should not be chosen smaller than $1/\sqrt{2}$, to avoid oscillatory behavior in the SOC control loop. Equation (B.5) gives the final expression for k_{SOC}.

$$k_{SOC} = \frac{W_{bat}}{4\varsigma^2 \eta_{bat}\eta_{EM}^{-sign(P_{EM})}\tau_{ICE}} \tag{B.5}$$

Appendix C

Driving Cycles

Given bellow is a short summary of the driving cycles used in thesis. Figure C.1 shows the six different driving cycles and Table C.1 contains data, such as duration, distance, average speed and maximum speed, for the cycles.

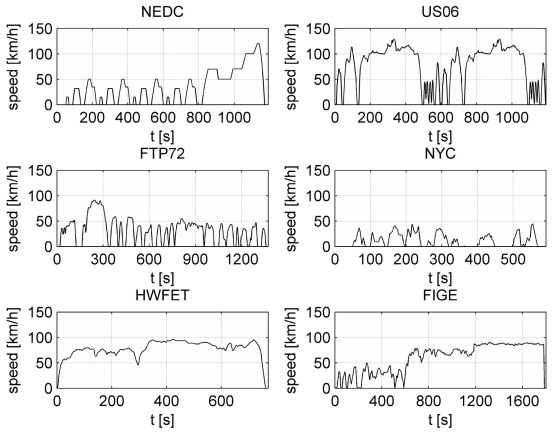

Figure C.1 The different driving cycles used in the thesis.

Table C.1 Driving cycles used for simulation in the thesis.

	Duration [s]	**Distance [km]**	**Max. Speed [km/h]**	**Average speed [km/h]**
NEDC	1180	11,0	120,0	33,4
US06[1]	600	12,9	129,2	77,2
FTP72	1369	12,1	91,2	31,5
NYC	598	1,89	44,6	11,4
HWFET	765	16,5	96,4	77,7
FIGE	1800	29,49	91,1	58,9

It should be pointed out that the US06 cycle shown in Figure C.1, consists of two US06 cycles, and it is this cycle that is used in the thesis when the US06 is referred to. The data for the cycle in Table C.1 is, however, only given for one cycle.